Shortwave Direct Radiative Effects of Above Cloud Aerosols Over Global Oceans Derived From Eight Years of CALIOP and MODIS Observations

Zhibo Zhang[1,2*], Kerry Meyer[3,4], Hongbin Yu[3,5], Steven Platnick[3], Peter Colarco[3], Zhaoyan Liu[6,7], Lazaros Oreopoulos[3]

1. Physics Department, University of Maryland Baltimore County (UMBC), Baltimore, Maryland, USA.
2. Joint Center of Earth System Technology (JCET), UMBC, Baltimore, Maryland, USA
3. NASA Goddard Space Flight Center, Greenbelt, Maryland, USA
4. Goddard Earth Science Technology and Research (GESTAR), Universities Space Research Association, Columbia, Maryland, USA
5. Earth System Science Interdisciplinary Center (ESSIC), University of Maryland, College Park, Maryland, USA
6. Science Systems and Applications, Inc. (SSAI)
7. NASA Langley Research Center, Hampton, Virginia, USA

Submitted to ACP for Publication

* Corresponding Author:
- Dr. Zhibo Zhang
- Email: Zhibo.Zhang@umbc.edu
- Phone: (410) 455-6315

Abstract:

In this paper, we studied the frequency of occurrence and shortwave direct radiative effects (DRE) of above-cloud aerosols (ACAs) over global oceans using eight years (2007~2014) of collocated CALIOP and MODIS observations. Similar to previous work, we found high ACA occurrence in four regions: Southeast (SE) Atlantic region where ACAs are mostly light-absorbing aerosols, i.e., smoke and polluted dust according to CALIOP classification, originating from biomass burning over African Savanna; Tropical Northeast Atlantic and Arabian Sea where ACAs are predominantly windblown dust from the Sahara and Arabian desert, respectively; and Northwest Pacific where ACAs are mostly transported smoke and polluted dusts from Asian. From radiative transfer simulations based on CALIOP-MODIS observations and a set of the preselected aerosol optical models, we found the DREs of ACAs at the top of atmosphere (TOA) to be positive (i.e., warming) in the SE Atlantic and NW Pacific regions, but negative (i.e., cooling) in TNE Atlantic and Arabian Sea. The cancellation of positive and negative regional DREs results in a global ocean annual mean diurnally averaged cloudy-sky DRE of 0.015 W/m^2 (range of −0.03 to 0.06 W/m^2) at TOA. The DREs at surface and within atmosphere are −0.15 W/m^2 (range of −0.09 to −0.21 W/m^2), and 0.17 W/m^2 (range of 0.11 to 0.24 W/m^2), respectively. The regional and seasonal mean DREs are much stronger. For example, in the SE Atlantic region the JJA (July ~ August) seasonal mean cloudy-sky DRE is about 0.7 W/m^2 (range of 0.2 to 1.2 W/m^2) at TOA. All our DRE computations are publicly available[†]. The uncertainty in our DRE computations is mainly

[†]https://drive.google.com/folderview?id=0B6gKx4dgNY0GMVYzcEd0bkZmRmc&usp=sharing

cause by the uncertainties in the aerosol optical properties, in particular aerosol absorption, the uncertainties in the CALIOP operational aerosol optical thickness retrieval, and the ignorance of cloud and potential aerosol diurnal cycle. In situ and remotely sensed measurements of ACA from future field campaigns and satellite missions, and improved lidar retrieval algorithm, in particular vertical feature masking, would help reduce the uncertainty.

1. Introduction

Although most tropospheric aerosols are emitted into the atmospheric boundary layer, they can be convectively lifted above low-level clouds, or in some cases are emitted at altitudes higher than the boundary layer and are subsequently transported over low-level cloud decks. In fact, above-cloud aerosols (ACA) have been observed in several regions of the globe (Devasthale and Thomas, 2011; Winker et al., 2013). ACA is an important component of the climate system because its interactions (scattering and absorption) with shortwave (SW) solar radiation (so-called direct radiative effect) could differ substantially from that of clear-sky aerosols or below cloud aerosols, particularly for absorbing particles. In this study we focus only on the SW direct radiative effect (DRE), which for clarity we will refer to as DRE for short. The DRE of aerosols at the top of the atmosphere (TOA) is strongly dependent on the underlying surface. Over dark surfaces the scattering effect of aerosols is generally dominant, leading to a negative DRE (i.e., cooling) at TOA. In contrast, when aerosols reside above clouds, aerosol absorption of solar radiation can be significantly enhanced by cloud reflection, which can offset or even exceed the scattering effect of the aerosol (depending on the aerosol radiative properties) and can yield a less negative or even positive (i.e., warming) DRE at TOA (Abel et al., 2005; Chand et al., 2009; Keil and Haywood, 2003; Meyer et al., 2013; Zhang et al., 2014). The larger the cloud reflection, the more likely the positive DRE will occur. Thus, an accurate quantification of ACA DRE is needed to improve the understanding of aerosol effects on the radiative energy balance and climate. In the past decade, the DRE of aerosols in clear-sky conditions has been well studied and relatively well constrained by satellite and in situ data (Yu et al., 2006). However, because

72 traditional aerosol remote sensing techniques, in particular those using passive sensors,
73 are limited only to clear-sky conditions, the DRE of ACA had been largely unexplored
74 until recently. Moreover, model simulations of ACA DRE show extremely large
75 disparities (Schulz et al., 2006).

76 Recent advances in active and passive remote sensing techniques have filled this
77 data gap and have provided an excellent opportunity for studying the DRE of ACA (Yu
78 and Zhang, 2013). The Cloud-Aerosol Lidar with Orthogonal Polarization (CALIOP)
79 onboard NASA's Cloud-Aerosol Lidar and Infrared Pathfinder Satellite Observations
80 (CALIPSO) satellite was launched in 2006 as part of NASA's A-Train satellite
81 constellation (Stephens et al., 2002; Winker et al., 2007). As an active lidar with
82 depolarization and two wavelengths, CALIOP is able to measure the vertical distribution
83 of aerosol backscatter, extinction, particle depolarization ratio, and color ratio for clear-
84 sky aerosols, ACA, and aerosol below thin high-level clouds. These measurements,
85 combined with cloud observations from CALIOP itself and other A-train instruments
86 have provided a revolutionary global view of the vertical distribution of aerosols and
87 clouds (e.g., Winker et al., 2013). In addition to vertical feature masking, CALIOP also
88 provides operational retrievals of a variety of aerosol properties, such as aerosol type
89 classification, aerosol layer height, aerosol optical thickness (AOT), and aerosol
90 extinction profile, for both clear-sky aerosols and ACA.

91 Although CALIOP is the first to provide quantitative measurements of ACA on
92 an operational basis, its narrow along-track sampling leaves large spatial gaps in the
93 observations. In recent years, several attempts have been made to detect ACAs and
94 retrieve their properties from passive imagers with much better spatial sampling than

CALIOP. Waquet et al. (2009) developed a method based on multi-angular polarization measurements from the Polarization and Directionality of the Earth Reflectances (POLDER) to retrieve above-cloud aerosol optical thickness (AOT) (Waquet et al., 2013a). Torres et al. (2011) developed an algorithm of simultaneously retrieving ACA properties for smoke and cloud optical thickness (COT) from ultraviolet (UV) aerosol index (AI) derived from the Ozone Mapping Instrument (OMI). Jethva et al. (2013) retrieved simultaneously the above-cloud AOT and COT from the spectral dependence of visible and near-infrared cloud reflectance as observed by the Moderate Resolution Imaging Spectroradiometer (MODIS). Similarly, Meyer et al. (2015) developed a multispectral optimal inversion technique to retrieve ACA AOT, COT, and cloud effective particle radius (CER) from MODIS. A review of the emerging satellite-based ACA observations can be found in (Yu and Zhang, 2013). These emerging techniques based on passive sensors will provide insights into ACA and their radiative effects over much broader regions in the future. At present, however, they are primarily at the research level and no operational data are yet available.

The ACA DRE can be calculated with radiative transfer models using the retrieved ACA AOT, COT, and preselected aerosol optical properties. This approach is referred to as the forward calculation method. Chand et al. (2009) aggregated CALIOP above-cloud AOT retrievals (Chand et al., 2008) and Terra MODIS cloud products to monthly means at 5ºx5º grids and calculated the radiative effects of transported smoke above the low-level stratocumulus deck in the SE Atlantic. This spatial-temporal aggregation of the satellite data obscures the potential influence of cloud and aerosol sub-grid variability on the DRE, which could lead to significant uncertainty (Min and Zhang,

2014). The use of operational MODIS COT could also bias the DRE low (less positive or more negative) because of the low bias of MODIS COT induced by overlying light-absorbing aerosols (Coddington et al., 2010; Haywood et al., 2004). In Meyer et al. (2013), the MODIS COT bias due to ACA contamination was corrected using collocated CALIOP above-cloud AOT observations, and the unbiased MODIS cloud properties and CALIOP above-cloud AOT were used to calculate pixel-level cloudy sky ACA DRE. Such rigorous collocation has an obvious advantage as it takes into account the spatial-temporal variability of clouds and aerosols. However, it is computationally expensive and requires large amounts of pixel-level data. Recently, Zhang et al. (2014) developed a novel statistical method of computing ACA DRE based on the fact that ACA AOT and COT are generally randomly overlapped. This method greatly improves the ACA DRE computation efficiency while maintaining the same level of accuracy as the pixel-level computations. The high efficiency of this method enables us to compute 8 years of ACA DRE over global oceans in this study.

In the forward calculation approach discussed above, the DRE depends on the selection of aerosol optical properties, in particular the single scattering albedo. Alternatively, other approaches allow for bypassing the aerosol optical property assumption. For example, Peters et al. (2011), Wilcox (2012), and more recently (Feng and Christopher, 2015) estimated the DRE of ACA through regression of multiple satellite data sets from the A-Train, including OMI UV AI, CERES (Clouds and the Earth's Radiant Energy System), and AMSER-E (Advanced Microwave Scanning Radiometer for EOS). de Graaf et al. (2012) developed a method that takes advantage of the wide spectral coverage of the space-borne Scanning Imaging Absorption

Spectrometer for Atmospheric Chartography (SCIAMACHY). They first inferred cloud parameters (e.g., COT and CER) from the SCIAMACHY observations in the short-wave infrared region (i.e., 1.2 μm and 1.6 μm) where the impact of ACA on cloud reflectance is generally minimal. Then, they estimate the DRE from the difference between the SCIAMACHY observed cloud reflectance spectrum (i.e., polluted) and that of a computed (i.e., clean) spectrum derived from the inferred cloud parameters. These studies thus minimized the impact of aerosol retrieval uncertainty in the DRE estimate. On the other hand, these studies only provided estimates of the *instantaneous* DRE of ACA at the satellite crossing time and only at TOA, which is often not adequate for climate studies and model evaluations. DRE at surface and within the atmosphere are required to assess the full impact of aerosols on climate, and models often report diurnally averaged DRE.

Although the abovementioned studies have shed important light on the radiative effects of ACA on the climate system, several aspects of ACA remain unexplored. First, there is a lack of a global and multiyear perspective since almost all previous studies have focused on the SE Atlantic Ocean and over a limited time period. Second, most studies have only reported instantaneous DRE at TOA, which is not adequate for climate studies and model evaluations. In addition, the impact of retrieval uncertainties in satellite products (e.g., CALIOP aerosol and MODIS cloud products) on computed DRE has not been sufficiently assessed.

The objective of this study is to derive estimates of the diurnally averaged DRE of ACA over global oceans from collocated CALIOP and MODIS observations over 8 years (2007-2014). This is the first observation-based study (as far as we are aware) that

provides a global and multiyear perspective of the DRE of ACA. In addition to the DRE at TOA, we also calculate the DRE of ACA at the surface and within the atmosphere. The diurnal variation of solar radiation is fully accounted for in this study, making our results more directly comparable to the model reports of the diurnally averaged DRE, though it is important to note that the diurnal variation of the underlying cloud properties are not considered. Moreover, we carried out a series of sensitivity tests to estimate the impact of the uncertainties associated with aerosol scattering properties and satellite retrieval bias on the DRE results. The rest of this paper is organized as follows: Section 2 describes the satellite products used to derived the global distribution of ACA; Section 3 discusses the global distribution and seasonal variability of ACA; Section 4 briefly overviews the method used to derive the DRE of ACA; and Section 5 details the results. The major uncertainties in DRE computation are assessed in Section 6. The main findings and conclusions are summarized in Section 7.

2. Satellite Data

In this study, we use the CALIOP Version 3 level-2 aerosol and cloud layer products to derive the statistics of ACA properties and the MODIS Collection 6 (C6) level-3 daily gridded cloud product for cloud property statistics. This section provides a brief overview of these products, including the potential biases and uncertainties.

2.1. CALIOP

The CALIOP Version 3 level-2 aerosol and cloud layer products (Winker et al., 2009), at a nominal 5 km horizontal resolution (product names “CAL_LID_L2_05kmALay” and

186 "CAL_LID_L2_05kmCLay"), are used to first identify ACA pixels, and then to derive
187 aerosol layer properties, including aerosol type, AOT, and layer top and bottom height.
188 The CALIOP level-2 retrieval algorithm detects aerosol and cloud layers, and records
189 their top and bottom heights and layer integrated properties using a "feature finder"
190 algorithm and cloud-aerosol discrimination (CAD) algorithm (Liu et al., 2009). The
191 detected aerosol layers are further classified into six sub-types (i.e., polluted continental,
192 biomass burning, desert dust, polluted dust, clean continental and marine) (Omar et al.,
193 2009) and the detected cloud layers are assigned different thermodynamic phases (Hu et
194 al., 2007) based on the observed backscatter, color ratio and depolarization ratio. The
195 extinction of an aerosol or cloud layer is derived from the attenuated backscatter profile
196 using *a priori* lidar ratios, pre-selected based on aerosol sub-type and cloud phase (Young
197 and Vaughan, 2008). In the case where clear air is available both above and below a layer,
198 a constrained retrieval is performed to derive the lidar ratio as well as the extinction and
199 backscatter coefficient for the layer.

200 The CALIOP lidar is known to have several inherent limitations. First, it has very
201 limited spatial sampling, providing observations only along its ground track. Thus
202 computing the DRE of ACA over a given latitude-longitude grid box necessarily requires
203 assuming that the aerosol property statistics retrieved by CALIOP along its track
204 represent the statistics over the whole grid box. Moreover, the limited spatial sampling
205 also inhibits the use of CALIOP to study the variations of ACA and its DRE at small
206 temporal (e.g., inter-annual variability) or spatial scales (e.g., smoke or dust outbreak
207 event). Another limitation of CALIOP is that its daytime aerosol retrievals generally have
208 larger uncertainty in comparison with nighttime retrievals caused by strong background

solar noise (Hunt et al., 2009). Some recent studies have noted significant differences between daytime and nighttime CALIOP aerosol property retrievals, in particular the AOT retrievals, which is partly caused by the solar background noise issue (Meyer et al., 2013; Winker et al., 2013). The impact of daytime vs. nighttime CALIOP aerosol retrieval differences on the DRE of ACA is investigated in the uncertainty analysis detailed in section 6.

In addition to the sampling limitations, several recent studies have found that CALIOP daytime AOT retrievals for ACA, in particular above-cloud smoke, are significantly smaller compared to collocated results from other techniques (Jethva et al., 2014; Torres et al., 2013; Waquet et al., 2013b) and results retrieved from the CALIOP level 1 data using an opaque water cloud (OWC) constrained technique (Liu et al., 2015). The cause for the bias is complex and multiple sources can contribute to the AOT retrieval uncertainties (Liu et al., 2015), but the main issue is the failure of the current CALIOP retrieval algorithm to detect the full physical thickness of dense smoke layers. Smoke aerosol generally has a large attenuation at 532 nm that is 2-3 times larger than that at 1064 nm. The current CALIOP algorithms detect features based solely on the 532 nm data. Strong attenuation in dense smoke layers can make the detection of the true base of dense smoke layers very difficult. (This may be improved largely if the feature detection is performed at both 532 nm and 1064 nm.) As a result, the current CALIOP feature detection algorithm often fails to detect the full extent of dense aerosol layers, leading to low biases in retrieved AOT (Jethva et al., 2014; Liu et al., 2015; Torres et al., 2013). This underestimation of AOT apparently can have significant impact on the DRE computation. We have developed a simple method to estimate the upper limit of this

232 impact, which is detailed in section 6.

233 ### *2.2. MODIS*

234 In this study, we use the Collection 6 (C6) level-3 gridded daily Atmosphere product
235 from Aqua-MODIS (product name MYD08_D3) for the statistics of cloud properties and
236 other parameters, such as solar zenith angle, needed for ACA DRE computations. The
237 MYD08_D3 product contains gridded scalar statistics and histograms computed from the
238 level-2 (i.e., pixel-level) MODIS products. As summarized in (Platnick et al., 2003), the
239 operational level-2 MODIS cloud product provides cloud masking (Ackerman et al.,
240 1998), cloud top height retrieval based on CO_2 slicing or the infrared window method
241 (Menzel et al., 1983), cloud top thermodynamic phase determination (Baum et al., 2012;
242 Marchant et al., 2015; Menzel et al., 2006), and cloud optical and microphysical property
243 retrieval based on the bi-spectral solar reflectance method (Nakajima and King, 1990).
244 Level-3 aggregations include a variety of scalar statistical information (mean, standard
245 deviation, max/min occurrences) and histograms (marginal and joint) (Hubanks et al.,
246 2008). A particularly useful level-3 cloud product for this study is the daily joint
247 histogram of COT vs. cloud top pressure (CTP), derived using daily counts of successful
248 daytime level-2 pixel retrievals that fall into each joint COT-CTP bin. Eleven COT bins,
249 ranging from 0 to 100, and 13 CTP bins, ranging from 200 to 1000 mb, comprise the
250 histogram. As discussed below, the COT-CTP joint histogram allows for identification of
251 the portion of the cloud population that lays beneath the aerosol layer found by CALIOP,
252 as well as the corresponding COT probability distribution needed for DRE estimation. In
253 addition to the COT-CTP joint histogram, we also use the gridded mean solar and sensor
254 zenith angles for calculating instantaneous DRE and correcting the COT bias due to the

255 presence of ACA.

256 A major issue with MODIS data for ACA DRE computation is the potential COT
257 retrieval bias in the presence of significant overlying ACA. As noted in several previous
258 studies, an overlying layer of light-absorbing aerosol, e.g., smoke, makes the scene
259 appear darker than the otherwise clean cloud. This cloud-darkening effect often leads to a
260 significant underestimate of MODIS COT for scenes with smoke overlying clouds (e.g.,
261 Coddington et al., 2010; Haywood et al., 2004; Meyer et al., 2013). A fast COT
262 correction scheme has previously been developed (Zhang et al., 2014) to account for the
263 COT retrieval bias due to ACA, which is briefly overviewed in section 4.3.

264

265 ## *3. Global distribution of ACA*

266 The present study is limited to ocean scenes only. This decision was made for a
267 number of reasons. First, ACA occurs much more frequently over ocean than over land
268 (see Figure 3 of (Devasthale and Thomas, 2011)). Second, the contrast between ACA
269 DRE and clear-sky aerosol DRE is generally larger over ocean than over land because the
270 contrast between the ocean surface and cloud is larger than the contrast between the land
271 surface and cloud. Finally, the large spatial and spectral variability of land surface
272 reflectance makes the radiative transfer computation much more complicated than that
273 over the ocean. For these reasons, we limit our analysis only to global oceans and leave
274 the DRE of ACA over land for future study.

3.1. ACA identification and classification

The following criteria are used to identify ACA columns within the CALIOP 5km layer products: (1) the CALIOP 5km cloud layer product identifies at least one layer of liquid phase cloud in the profile; (2) the CALIOP 5km aerosol layer product identifies at least one layer of aerosol in the profile; (3) the "Layer_Base_Altitude" of the lowest aerosol layer is higher than the "Layer_Top_Altitude" of the highest cloud layer. The last criterion excludes some complicated scenarios, such as aerosol layers in between low and high level clouds, while retaining the majority of ACA cases. Following the best practice advice of the CALIOP science team (Winker et al., 2013), we used various data quality assurance metrics and flags to screen out low-confidence aerosol layers. Specifically, we only accept ACA layers having: (i) Cloud Aerosol Discrimination score values for the identified aerosol layer between −20 to −100; (ii) Extinction QC values of 0 or 1; and (iii) Feature Optical Depth Uncertainty smaller than 99.9. Any columns that do not satisfy the above criteria were classified as either clear sky if no cloud is found in the column or "clean" cloud if one or more cloud layers are present.

After ACA identification, we further classify the ACA layer into the six aerosol sub-types (i.e., Clean Marine, Dust, Polluted Continental, Clean Continental, Polluted Dust and Smoke) provided by the CALIOP product (Omar et al., 2009). The classification is needed later to select the aerosol optical properties to be used in the DRE computation. It should be noted that the CALIOP operational algorithm often identifies different sub-types for vertically adjacent aerosol layers (Meyer et al., 2013). Recent studies indicate that this is a misclassification issue in the current CALIOP operational algorithm (Liu et al., 2015; Meyer et al., 2013). Uncertainty in aerosol classification by

CALIOP operational algorithms is also highlighted in comparisons to airborne High Spectral Resolution Lidar (HSRL) observations, which retrieve directly the aerosol lidar ratio (Burton et al., 2013). These observations suggest highest uncertainty in aerosol typing for smoke and polluted dust cases. Aerosol type misclassification where CALIOP operational algorithms identify polluted dust is also highlighted in a recent study in which aerosol transport model fields are used to directly simulate the CALIOP aerosol typing and compared to native aerosol fields within the model (Nowottnick et al., 2015). In this study, we associate all ACA layers in a single profile with only one sub-type, namely the sub-type of the layer with the largest AOT. This classification scheme reduces the complication caused by aerosol misclassification in radiative transfer simulations.

3.2. Occurrence Frequency of ACA

After the identification of ACA cases in CALIOP data, we first investigate the geographical and seasonal variations of the occurrence frequency of ACA over global oceans. It should be noted that clouds can have a strong diurnal cycle, thus the occurrence frequency of ACA might also have a significant diurnal cycle. Unfortunately, because CALIOP is in a sun-synchronous polar orbit, it can provide only two snapshots of this diurnal cycle over most of the globe (except for polar regions), one during daytime (i.e., ascending local equatorial crossing time 1:30PM) and the other during nighttime (i.e., descending local equatorial crossing time 1:30AM). Here we define the ACA occurrence frequency (f_{ACA}) in a latitude-longitude box as the ratio of ACA columns to total cloudy columns sampled by CALIOP:

$$f_{ACA}\left(t^*\right)=\sum_{i=1}^{6} f_{ACA,i}\left(t^*\right)=\sum_{i=1}^{6}\frac{N_{ACA,i}}{N_{cloudy}}, \quad (1)$$

where t^* signifies that the f_{ACA} is observed at the CALIOP crossing time; $f_{ACA,i}$ is the fraction of cloudy columns covered by the i^{th} type of aerosol, N_{cloudy} is the total number of cloudy columns sampled by CALIOP within the grid, and $N_{ACA,i}$ is the number of ACA columns that have been identified as the i^{th} type of aerosol by CALIOP. This is different from the definition in (Devasthale and Thomas, 2011), in which the occurrence frequency is defined as the ratio of ACA columns to the total number of CALIOP observations. As such, the two definitions differ by a factor of f_c, the total cloud fraction. We define the occurrence frequency in this way because the f_{ACA} provides information additional to and independent of the total cloud fraction f_c that can help, for example, modelers understand whether an inadequate simulation of ACA is due to cloud and/or aerosol simulation. On the other hand, one has to couple our f_{ACA} together with f_c to depict a complete picture.

Figure 1 and 2 show the seasonal variation of total cloud fraction f_c and f_{ACA}, respectively, over global ocean derived from daytime CALIOP observations. There are several ACA frequency "hotspots" that can be clearly seen in Figure 2, from which four primary ACA regions can be defined (see Table 1). The types of ACA in each region according to the CALIOP aerosol classification product are shown in Figure 3.

1) SE Atlantic Ocean: This region is perhaps the most prominent ACA region during the boreal summer (JJA) and fall (SON) seasons (Figure 2c and d). The ACA over

the SE Atlantic primarily originates from the seasonal burning activities throughout the African Savanna (Eck et al., 2013; Ichoku et al., 2003; Myhre et al., 2003). Prevailing easterly winds in the free troposphere during this season often transport the biomass burning aerosols to the west, off the continent and over the ocean (Matichuk et al., 2007; Swap et al., 1996), where extensive marine boundary layer clouds persist for most of the year leading to a near-persistent seasonal smoke layer above the stratocumulus deck. As shown in Figure 3a, the ACAs in this region are primarily a mix of smoke and polluted dust.

2) Tropical Northeastern (TNE) Atlantic: During boreal spring (MAM) and summer (JJA) (Figure 2b and c), the dry and dust-laden Saharan Air Layer overlies the cooler, more-humid and cloudy tropical Atlantic Ocean. Not surprisingly, dust is the dominant type of ACA in this region as shown in Figure 3b.

3) Arabian Sea: During the Asian monsoon season (JJA), the cloud fraction increases to more than 90%, setting the stage for ACA from the transported dust aerosols from the surrounding deserts.

4) Northwestern (NW) Pacific Ocean: During the springtime, the industrial pollution and dust aerosols from Asia carried by the jet stream can travel thousands of miles to the NW Pacific Ocean where cloud fraction is high throughout the year. ACA in this region is a mixture of smoke, dust and polluted dust.

4. Methodology for computing ACA DRE

After the identification of ACAs, we use the method described in (Zhang et al., 2014) to calculate shortwave ACA DRE by using MODIS observations of clouds. This section provides a brief review the key features of this method.

4.1. Definitions of DRE

For a given latitude-longitude grid box, the grid-mean diurnally averaged shortwave all-sky aerosol radiative effect $\overline{\langle DRE_{all-sky} \rangle}$ is given by:

$$\overline{\langle DRE_{all-sky} \rangle} = \frac{1}{24} \int_{t_{\text{sunrise}}}^{t_{\text{sunset}}} \left[1 - f_c(t)\right] \langle DRE_{clear-sky}\left[\tau_a(t), \theta_0(t)\right] \rangle dt + \frac{1}{24} \int_{t_{\text{sunrise}}}^{t_{\text{sunset}}} f_c(t) \langle DRE_{cloudy-sky}\left[\tau_c(t), \tau_a(t), \theta_0(t)\right] \rangle dt \quad (2)$$

where the upper bar "¯" indicates the diurnal average and the angle bracket "$\langle\ \rangle$" indicates spatial average over the grid box; $f_c(t)$ is the instantaneous cloud fraction, and $\langle DRE_{clear-sky}(t) \rangle$ and $\langle DRE_{cloudy-sky}(t) \rangle$ are the hourly instantaneous DRE averaged over the clear-sky and cloudy-sky region of the grid, respectively. Note that in this study we compute the instantaneous DREs every hour during daytime to capture the diurnally variation of solar radiation. This is why the normalization factor is 1/24 in Eq. (2) and it needs to be changed accordingly if the instantaneous DREs are computed at a different frequency. For shortwave DRE, the integration range is from local sunrise hour t_{sunrise} to local sunset hour t_{sunset}, because the DRE during nighttime is zero. Note that the instantaneous $\langle DRE_{clear-sky}(t) \rangle$ is mainly dependent on AOT $\tau_a(t)$ and solar zenith angle

376 $\theta_0(t)$. In addition to τ_a and θ_0, $\langle DRE_{cloudy-sky}(t)\rangle$ is also dependent on the COT $\tau_c(t)$.
377 As pointed out in (Min and Zhang, 2014), in addition to $\theta_0(t)$, $f_c(t)$, $\tau_a(t)$, and $\tau_c(t)$
378 can also have a significant diurnal cycle that influences the diurnal average. However, the
379 orbit of CALIOP only allows it to provide a single snapshot of the diurnal cycle during
380 daytime (another during night time). Because of this limitation, we omit the diurnal
381 variation of $f_c(t)$, $\tau_a(t)$ and $\tau_c(t)$, and only use the value at the daytime CALIOP
382 crossing time t^*. Nevertheless, we still consider the diurnal variation of solar flux
383 associated by the change of $\theta_0(t)$. In such an approximation, we can rewrite the
384 $\overline{\langle DRE_{all-sky}\rangle}$ as follows:

385 $$\overline{\langle DRE_{all-sky}\rangle} \approx \left[1 - f_c(t^*)\right]\overline{\langle DRE^*_{clear-sky}\rangle} + f_c(t^*)\overline{\langle DRE^*_{cloudy-sky}\rangle}, \quad (3)$$

386 where the t^* corresponds to the daytime CALIOP crossing time (usually 1:30PM local
387 time), $\overline{\langle DRE^*_{clear-sky}\rangle}$ and $\overline{\langle DRE^*_{cloudy-sky}\rangle}$ are approximate clear-sky and cloudy-sky
388 aerosol DRE. In particular, $\overline{\langle DRE^*_{cloudy-sky}\rangle}$ can be integrated from the hourly
389 instantaneous DRE as:

390 $$\overline{\langle DRE^*_{cloudy-sky}\rangle} = \frac{1}{24}\int_{t_{\text{sunrise}}}^{t_{\text{sunset}}} \left\langle DRE_{cloudy-sky}\left[\tau_c(t^*), \tau_a(t^*), \theta_0(t)\right]\right\rangle dt\,, \quad (4)$$

391 where the normalization factor 1/24 is to obtain diurnal mean from hourly computations.
392 Theoretically, cloudy-sky aerosol DRE should include the contributions from aerosols in
393 all conditions, e.g., above, below or in-between clouds. However, it is difficult to
394 measure aerosol properties below clouds from space-borne instruments. Here we simply
395 assume cloudy-sky aerosol DRE is mainly attributed to ACAs. This is a reasonable

assumption for TOA DRE, but might introduce large uncertainties to surface and atmospheric DRE. The uncertainty caused by this assumption will be left for future study. Based on this assumption, we can rewrite Eq. (4) as

$$\begin{aligned}\overline{\left\langle DRE^{*}{}_{cloudy-sky}\right\rangle} &= f_{ACA}\left(t^{*}\right)\overline{\left\langle DRE^{*}{}_{ACA}\right\rangle} \\ &= f_{ACA}\left(t^{*}\right)\frac{1}{24}\int_{t_{\text{sunrise}}}^{t_{\text{sunset}}}\left\langle DRE_{ACA}\left[\tau_{c}\left(t^{*}\right),\tau_{a}\left(t^{*}\right),\theta_{0}(t)\right]\right\rangle dt\end{aligned}, \tag{5}$$

where $f_{ACA}\left(t^{*}\right)$ is the occurrence frequency of ACA observed at the CALIOP crossing time defined in Eq. (1). An important implicit assumption in Eq. (5) is that when CALIOP cannot detect an aerosol layer, the DRE is essentially zero. Using Eq. (5) we can derive the DRE at TOA $\overline{\left\langle DRE^{*}{}_{cloudy-sky}\right\rangle}_{TOA}$ and at the surface $\overline{\left\langle DRE^{*}{}_{cloudy-sky}\right\rangle}_{surface}$. The DRE within the atmosphere $\overline{\left\langle DRE^{*}{}_{cloudy-sky}\right\rangle}_{atm}$ is calculated as follows:

$$\overline{\left\langle DRE^{*}{}_{cloudy-sky}\right\rangle}_{atm} = \overline{\left\langle DRE^{*}{}_{cloudy-sky}\right\rangle}_{TOA} - \overline{\left\langle DRE^{*}{}_{cloudy-sky}\right\rangle}_{surface}. \tag{6}$$

Here, it is necessary to point out that what is often reported in previous studies is the instantaneous DRE observed at the CALIOP (or other satellite such as SCIAMACHY) crossing time and averaged over only ACA pixels, namely, $\left\langle DRE_{ACA}\left[\tau_{c}\left(t^{*}\right),\tau_{a}\left(t^{*}\right),\theta\left(t^{*}\right)\right]\right\rangle$. This quantity has obvious limitations (e.g., diurnal variation is ignored) and can be misleading if not accompanied by f_{ACA}, because different instruments or algorithms might have different sensitivities or even definitions of ACA (e.g., OMI AI index vs. CALIOP backscatter). In our view, the diurnally averaged, grid-mean, cloudy-sky DRE, $\overline{\left\langle DRE^{*}{}_{cloudy-sky}\right\rangle}$, is more suitable for inter-comparison, and also

414 more relevant for climate study and modeling evaluation, on which we shall focus in this
415 study.

416 *4.2. Computation of instantaneous DRE*

417 It is clear from Eq. (5), once the instantaneous $\left\langle DRE_{ACA}\left[\tau_c\left(t^*\right),\tau_a\left(t^*\right),\theta(t)\right]\right\rangle$ is
418 known one can easily derive $\overline{\left\langle DRE^*_{cloudy-sky}\right\rangle}$ from the integral. In this section, we explain
419 how the instantaneous DRE is computed from the CALIOP and MODIS products.
420 Hereafter we drop the time dependence for simplicity. As mentioned in Section 2.1, the
421 CALIOP operational algorithm classifies aerosol layers into 6 sub-types. Therefore, we
422 can rewrite $\left\langle DRE_{cloudy-sky}\right\rangle$ as:

423 $$\left\langle DRE_{cloudy-sky}\right\rangle = \sum_{i=1}^{6} f_i \left\langle DRE_{ACA}\right\rangle_i , \tag{7}$$

424 where $\left\langle DRE_{ACA}\right\rangle_i$ is the DRE of the i^{th} type of CALIOP aerosol (e.g., dust, smoke, etc.,
425 see Figure 3) and f_i is the frequency of detection of the i^{th} type of aerosol. To compute the
426 $\left\langle DRE_{ACA}\right\rangle_i$, one could collocate the level-2 CALIOP and MODIS data and compute the
427 DRE pixel-by-pixel as follows:

428 $$\left\langle DRE_{ACA}\right\rangle_i = \frac{1}{N_i}\sum_{j=1}^{N_i} DRE_{ACA}\left(\tau_{a,j},\tau_{c,j}\right), \tag{8}$$

429 where $\tau_{a,j}$ and $\tau_{c,j}$ are the ACA and cloud optical thicknesses of the j^{th} pixel,
430 respectively. Mathematically, Eq. (8) is equivalent to the following double integral:

431 $$\left\langle DRE_{ACA}\right\rangle_i = \int_0^{\infty}\left[\int_0^{\infty} DRE_{ACA}(\tau_a,\tau_c)P_i(\tau_a,\tau_c)\,d\tau_a\right]d\tau_c , \tag{9}$$

where $P_i(\tau_a,\tau_c)$ is the joint probability density function (PDF) of the above-cloud AOT of the i^{th} CALIOP aerosol type and below-aerosol COT. Deriving DRE from Eq. (9) or (8) requires large amounts of level-2 CALIOP and MODIS data and pixel-by-pixel collocation and radiative transfer simulations. It is thus too computationally expensive and cumbersome for multiyear global studies.

As shown in (Zhang et al., 2014), because the AOT of ACA is generally uncorrelated with the COT below, Eq. (9) can be simplified by assuming $P_i(\tau_a,\tau_c) = P_i(\tau_a)P(\tau_c)$ as:

$$\left\langle DRE_{ACA} \right\rangle_i = \int_0^\infty \left[\int_0^\infty DRE_{ACA}(\tau_a,\tau_c) P_i(\tau_a) d\tau_a \right] P(\tau_c) d\tau_c , \quad (10)$$

where $P(\tau_c)$ and $P_i(\tau_a)$ are the PDF of below-aerosol COT and above-cloud AOT (i^{th} CALIOP aerosol type), respectively. The advantage of Eq. (10) is that it allows $P(\tau_c)$ and $P_i(\tau_a)$ to be derived separately, thus tedious pixel-level collocation and pixel-by-pixel radiative transfer computations can be avoided. Following (Zhang et al., 2014), we derive $P_i(\tau_a)$ from the CALIOP level-2 aerosol layer product and $P(\tau_c)$ from the joint histogram of cloud optical thickness and cloud top pressure (COT-CTP joint histogram) in the MODIS daily level-3 product. In order to speed up the calculations, we use pre-computed aerosol type-specific look-up tables (LUTs) instead of online radiative transfer computation when deriving the $\left\langle DRE_{ACA} \right\rangle_i$. The DRE LUTs are computed using the RRTM-SW model (Clough et al., 2005; Iacono et al., 2008). For details about the computation of DRE LUTs readers are referred to (Zhang et al., 2014).

4.3. COT retrieval correction for DRE computation

When a cloudy pixel is contaminated by overlying light-absorbing aerosols the MODIS COT retrieval is generally biased low (Coddington et al., 2010; e.g., Haywood et al., 2004). This COT retrieval bias needs to be accounted for in radiative transfer computation to avoid biased DRE (Meyer et al., 2013). A simple and fast correction scheme has been developed (Zhang et al., 2014) to account for the COT retrieval bias due to ACA in our DRE computation. First, we derive a MODIS LUT for "contaminated" clouds, which is essentially same as the operational MODIS LUT except that we put a layer of ACA on top of the cloud in the radiative transfer simulations to account for the impact of ACA on cloud reflectance. Then, we project the observed cloud reflectance that is contaminated by ACA onto the "contaminated" LUT to determine the corrected COT. This process is essentially to shift the potentially biased MODIS $P(\tau_c)$ to a new "unbiased" PDF $P'(\tau_c)$ that is actually used in the DRE computation. It should be noted that because different aerosol types can have different impacts on the MODIS COT retrievals, the COT bias is dependent on the radiative properties of the ACA, and the correction process is therefore dependent on the assumed aerosol model. Hereafter, all DRE computations are based on the "unbiased" COT unless otherwise stated.

It is important to keep in mind that this COT correction scheme is only designed to account for the ACA-induced biases in the grid-level COT statistics. As shown in (Zhang et al., 2014), the DRE computations based on this simple scheme agree very well with results based on more rigorous pixel-level corrections. However, this statistical scheme is not intended for deriving the unbiased COT at pixel level. Interested readers can refer to

(Meyer et al., 2015) for a novel method to simultaneously retrieve the AOT of ACA and the unbiased COT and CER of the underlying cloud at the pixel level.

4.4. Aerosol optical properties

As shown in Figure 3, CALIOP-observed ACAs in the four ACA regions are primarily dust, smoke, and polluted dust aerosols. Given the AOT and underlying surface brightness, the DRE of aerosols is mainly determined by their optical properties, in particular single-scattering albedo. Therefore, the aerosol optical model assumption has a significant impact on the DRE results. In the control run shown in section 5, we choose to build our aerosol optical property models to be as consistent as possible to the models used in the operational CALIOP retrieval algorithm (Omar et al., 2009), with specifications given below.

1) Smoke: In the control run, we use the model described in (Omar et al., 2009) for smoke aerosols to be consistent with the CALIOP operational retrieval algorithm (referred to hereafter as "CALIOP smoke"). Figure 4a shows the optical properties of CALIOP smoke calculated using Mie code (Wiscombe, 1980), including extinction efficiency (Q_e), single-scattering albedo (ω) and asymmetry factor (g) for the fourteen RRTM SW bands. In the calculation, we assumed a bimodal lognormal size distribution and a single refractive index of $1.517+0.023i$ for all wavelengths (Omar et al., 2009). The band-averaged single-scattering albedo of CALIOP smoke is about 0.85 in the visible spectral region.

2) Dust: In the control run, the bulk scattering properties of dust aerosols shown in Figure 4c are calculated using the bimodal lognormal size distributions in (Omar et al., 2009) to be consistent with the operational CALIOP retrievals. For DRE computation, the refractive index over the whole solar spectrum is needed. However, in (Omar et al., 2009), the refractive index of dust is given only for the two wavelengths of CALIOP, i.e., 532nm and 1064nm. Alternatively, we use the dust spectral refractive index data reported in (Colarco et al., 2014) to combine with the size distributions in (Omar et al., 2009) to derive the optical properties of dust. (Colarco et al., 2014) evaluated the sensitivity of dust transport simulations in NASA's GEOS-5 climate model to dust particle shape and spectral refractive indices. Two sets of dust refractive indices are tested. One is a merger of remote sensing-based estimates of dust refractive indices in the shortwave (Colarco et al., 2002; Kim et al., 2011) with the (Shettle and Fenn, 1979) values in the longwave. Following (Colarco et al., 2014) we refer to this model hereafter as "OBS dust." The other one is based on the dust spectral refractive index provided in the OPAC database (OPAC (Hess et al., 1998)) (Colarco et al., 2014) (hereafter referred to as the "OPAC dust model"). The OPAC dust refractive index has been used for dust optical properties in previous studies by Perlwitz et al. (2001) and Colarco et al. (2010). In (Colarco et al., 2014), OBS dust model is found to yield better dust clear-sky radiative forcing simulations in comparison with satellite observation. Therefore, we choose to use the OBS dust model in the control run. The OPAC dust model is more absorptive than the OBS model, which will be used in the

uncertainty study to test the sensitivity of the DRE of above-cloud dust to its optical properties, in particular absorption.

3) Polluted dust: In the control run, we use the model described in (Omar et al., 2009) to compute the scattering properties, shown Figure 4e, of polluted dust aerosols identified by CALIOP. In the calculation, we assumed a bimodal lognormal size distribution and a single refractive index of 1.54+0.0019*i* for all wavelengths.

In order to estimate the sensitivity of DRE of ACAs to their optical properties, we carried out a series of sensitivity studies using different aerosol optical models. The results from these sensitivity studies are discussed in section 6.1.

5. Shortwave Cloudy-sky DREs due to ACA

5.1. Global and Seasonal Climatology

Figure 5 shows the seasonal mean diurnally averaged shortwave cloudy-sky DRE at TOA ($\overline{\left\langle DRE^{*}{}_{cloudy-sky}\right\rangle_{TOA}}$) derived from 8 years of MODIS and CALIOP data using the method described in the previous section. The computation uses the baseline optical models (i.e., "CALIOP smoke" and "OBS dust") described above. The regional and seasonal mean values are shown in Table 2. It is not surprising that the regions with significant cloudy-sky DRE coincide with the regions of high ACA occurrence frequency (Figure 2). Similar to previous studies, we found the cloudy-sky DRE in the SE Atlantic Ocean to be positive during the boreal summer (JJA) and fall (SON) seasons when the ACA is most active (Figure 3a). The annual mean cloudy-sky DRE at TOA in this region

538 is 0.21 W/m^2 (Table 2) and the seasonal mean is as large as 0.44 W/m^2 during SON. The
539 TOA DRE is negative in the TNE Atlantic Ocean (annual mean −0.78 W/m^2) and
540 Arabian Sea (annual mean −0.54 W/m^2), where ACA is predominantly dust (Figure 3b
541 and c). This result suggests that the above cloud dust tends to have a cooling effect on the
542 climate, similar to its clear-sky counterpart. The cloudy-sky DRE at TOA in the NW
543 Pacific region is mostly positive and quite small (annual mean 0.04 W/m^2), and is only
544 noticeable in the boreal spring season (MAM) along the coast of China (Figure 5b). Note
545 that these numbers are not directly comparable to many previous studies (e.g., de Graaf et
546 al., 2014; Feng and Christopher, 2015; Meyer et al., 2013), however, because the
547 previous results are either instantaneous DRE that do not consider the diurnal variation of
548 solar radiation, or are DRE averaged over only ACA pixels without accounting for the
549 near zero DRE from "clean" clouds (i.e., not the true cloudy-sky DRE). When averaged
550 over the global oceans, the positive DRE in the SE Atlantic is largely cancelled out by the
551 negative DRE of dust in the North Atlantic and Arabian Sea, leading to an overall TOA
552 DRE of about −0.02 W/m^2. Because most previous studies are focused on the SE
553 Atlantic region, we cannot find other studies for which to compare our global DRE
554 results. But we note that most AeroCom model simulations of global cloudy-sky aerosol
555 DRE reported in (Schulz et al., 2006) fall in the range of −0.10 ~ 0.05 W/m^2 (See their
556 Table 5), although we understand our study is fundamentally different from (Schulz et al.,
557 2006).

558 Despite the large difference in TOA DRE, the DRE of ACA at the surface
559 ($\overline{\left\langle DRE^{*}_{cloudy-sky} \right\rangle}_{surface}$) is always negative (Figure 6) and the DRE of ACA within

atmosphere ($\overline{\left\langle DRE^{*}_{cloudy-sky} \right\rangle_{atm}}$) is always positive (Figure 7), both as expected, in all of the active ACA regions. The annual mean cloudy-sky DREs at surface and within atmosphere averaged over global oceans are −0.13 and 0.11 W/m^2, respectively (Table 2).

The 8-year time series of monthly mean cloudy-sky DRE at TOA due to the three most prevalent ACA types classified by CALIOP—smoke, polluted dust and dust—are shown in Figure 8. As expected, the smoke ACA has a positive DRE with the peak value usually in September when the smoke is most active in the SE Atlantic region. The DRE of polluted dust ACA is generally positive, often with two peaks in the annual cycle—a larger one in boreal fall corresponding to the ACA active period in the SE Atlantic, and a smaller one usually in early boreal spring corresponding to the ACA active period in the NW Pacific. Together, the smoke and polluted dust have a combined annual mean DRE of about 0.03 W/m^2 at TOA (see Table 3). Considering that the operational CALIOP retrievals often underestimate the AOT of ACA, the real DRE might be significantly larger. In fact, in the sensitivity test discussed in section 6, the annual mean cloudy-sky TOA DRE from smoke and polluted dust can be up to about 0.06 W/m^2, which is comparable to the radiative forcing from light absorbing aerosols on snow and ice (IPCC AR5). The dust ACA has a strong negative TOA DRE with a peak magnitude usually in July corresponding to the heaviest dust period in the North Atlantic region (Figure 3b). On the basis of these global ocean time series, we did not observe significant inter-annual variability.

5.2. Regional analysis

5.2.1. SE Atlantic Ocean

As seen in Figure 3, the ACAs in the SE Atlantic region occur mostly during the dry season of the African Savanna (e.g. June to October) with peak frequency around August and September. According to CALIOP, the ACAs in this region consist mostly of smoke and polluted dust (Figure 3a) that have significant absorption effects as shown in Figure 4. Figure 9 provides an in-depth explanation of why the ACAs in this region generate a strong warming effect at TOA, as well as an insight into our method used for computing the DRE of ACA described in Section 4. The color contour in Figure 9 corresponds to the diurnally averaged DRE at TOA as a function of the AOT of ACA and the COT of the underlying cloud, i.e., the $DRE_{ACA}(\tau_a,\tau_c)$ term in Eq. (9). The general patterns for smoke and polluted dust are quite similar, i.e., DRE is generally positive and increases with both AOT and COT. On the other hand, polluted dust has a smaller DRE than smoke for a given AOT and COT combination. As described in Section 4, the $DRE_{ACA}(\tau_a,\tau_c)$ is pre-computed off-line and is stored in a LUT to accelerate the computation. To obtain the spatially averaged DRE, $\langle DRE_{ACA}\rangle$, we integrate $DRE_{ACA}(\tau_a,\tau_c)$ with respect to the joint PDF of AOT and COT (i.e., the line contours in Figure 9) that is derived from the CALIOP and MODIS observations as described in Section 4. As seen in Figure 9a, during JJA the PDF of AOT has a peak slightly larger than 0.1 at 532nm. The COT PDF has two peaks, one around 3 and the other around 10. Compared to smoke, polluted dust in Figure 9b has a smaller AOT with the PDF peaking

601 at AOT slightly smaller than 0.1. The smaller AOT and weaker absorption together lead
602 to a smaller DRE of polluted dust compared to smoke, as seen in Figure 8.

603 Figure 10 tells a similar story as Figure 9, but from a different perspective. Here,
604 we plotted the grid-mean DRE of ACA at TOA as a function grid-mean AOT of ACA
605 based on observations from the SE Atlantic region. To show the importance of COT in
606 modulating the ACA DRE we classify the data into three grid-mean COT bins, as
607 indicated by the colors in the figure. In addition to the expected increase of DRE with
608 AOT, we also notice that the slope of the DRE with respect to AOT, i.e., the DRE
609 efficiency, generally increases with increasing grid-mean COT. The DRE efficiency for
610 smoke is 17.9, 22.6 and 28.6 W/m^2/AOT for COT less than 4, COT between 4 and 8, and
611 COT greater than 8, respectively. The corresponding DRE efficiency for polluted dust is
612 much smaller, yielding 6.7, 13.6, and 16.6 W/m^2/AOT, respectively. This result is not
613 surprising given the $DRE_{ACA}(\tau_a,\tau_c)$ pattern in Figure 9 and has also been noted in
614 several pervious studies (Meyer et al., 2013; Yu et al., 2010; Zhang et al., 2014).
615 Nevertheless, it highlights the importance of cloud optical thickness (i.e., brightness) in
616 determining the DRE efficiency of ACA.

617 Finally, Figure 11 summarizes the multiyear seasonal meant ACA and cloud
618 properties, as well as the DRE of ACA, in the SE Atlantic region during JJA. The
619 seasonal mean total AOT of ACA at 532nm (Figure 11a), including all types of aerosols,
620 is mainly between 0.1 to 0.2, with largest values found over the coastal region and
621 reducing gradually toward the open sea presumably as a result of dry and/or wet
622 deposition of smoke. The pattern of COT in Figure 11b is more homogeneous (mostly
623 between 6~8) except for a region of large values (around 10) along latitude 10° S. Given

624 the strong dependence of DRE on AOT in Figure 9 and Figure 10, it is not surprising to
625 see that the seasonal mean cloudy sky DRE of ACA in the SE Atlantic region (Figure
626 11c) largely resembles the pattern of AOT (Figure 11a). In contrast, the DRE efficiency
627 in Figure 11d aligns more with the COT pattern in Figure 11b, as one would expect given
628 the results in Figure 10.

629 ### *5.2.2. TNE Atlantic Ocean and Arabian Sea*

630 As discussed in Section 5.1, the TNE Atlantic Ocean and Arabian Sea are another
631 two regions with high occurrence frequency of ACA (Figure 2). As shown in Figure 3,
632 dust aerosols are the dominant type of ACA in both regions with a general cooling effect
633 at TOA (Figure 5). An analysis similar to Figure 9 and Figure 10 but for the dust aerosols
634 in the TNE Atlantic region and Arabian Sea is shown in Figure 12. A comparison of
635 Figure 12a with Figure 9 reveals several important differences between the dust ACA-
636 dominated region and the SE Atlantic smoke region. The color map in Figure 12a reveals
637 that above cloud dust with the optical properties in Figure 4c in general has a cooling
638 effect at TOA for COT smaller than about 7. When the cloud becomes optically thicker,
639 the DRE of above cloud dust at TOA switches sign to a warming effect. The line contour
640 in Figure 12a reveals that most of the clouds found in the TNE Atlantic region during JJA
641 have a COT smaller than 10. As a result, the grid-mean DRE of ACA at TOA in this
642 region is mostly negative as seen in both Figure 12b and previously in Figure 5. It is
643 interesting to note that the PDF of the AOT of above cloud dust has a peak value around
644 0.3 in Figure 12a, which is larger than both the smoke and polluted dust in the SE
645 Atlantic. This result reiterates the fact reported in many previous studies, that the sign of
646 aerosol DRE at TOA is primarily determined by aerosol absorption, in particular with

647 respect to the underlying surface, rather than aerosol loading. Similar to Figure 10, we
648 found in Figure 12b that the grid-mean DRE in the TNE Atlantic region has a strong
649 dependence on AOT, i.e., the magnitude of the negative DRE increases with increasing
650 AOT. However, we found little dependence of grid-mean ACA DRE on grid-mean COT
651 in Figure 12b in contrast to the case of smoke or polluted dust in Figure 10. This result
652 indicates that the grid-mean COT is not very revealing about the DRE of above-cloud
653 dust. The overall DRE efficiency of above-cloud dust in this region based on grid-level
654 statistics is −29.3 W/m^2/AOT. The analysis for Arabian Sea in Figure 12c and d turns out
655 to be very similar to the TNE Atlantic region. The overall DRE efficiency of above-cloud
656 dust in the Arabian Sea region is −28.4 W/m^2/AOT. This result implies that the
657 difference in the cloud-sky DRE between the TNE Atlantic and Arabian Sea is mainly
658 caused by the difference in ACA occurrence frequency f_{ACA} rather than aerosol or cloud
659 property difference. For example, the JJA seasonal mean TOA DRE is −2.39 W/m^2 in
660 TNE Atlantic vs. −0.97 W/m^2 in the Arabian Sea. This difference is mainly caused by the
661 fact that the TNE Atlantic has a higher f_{ACA} around 0.4 than Arabian Sea around 0.15
662 (Figure 3).

663 ### *5.2.3. NW Pacific Ocean*

664 The ACA in the NW Pacific Ocean has a small positive DRE at TOA, with a
665 regional annual mean of only 0.04 W/m^2 (Table 2). The positive DRE is primarily due to
666 smoke and polluted dust aerosols (see Figure 3 and Figure 13). Note that CALIOP
667 observes significantly more ACA in the NW Pacific region during nighttime (See Figure
668 2 in the supplementary material) than it does during daytime (Figure 2). If this difference
669 is due to CALIOP instrument issues (i.e., low signal-to-noise-ratio during daytime), it is

then likely that the TOA DRE in Table 2 for the NW Pacific region is substantially underestimated. In section 6, we estimated the impact of daytime vs. nighttime CALIOP aerosol retrieval differences on ACA DRE. Indeed, we found that the TOA DRE in the NW Pacific Ocean region significantly increases if nighttime CALIOP retrievals are used in DRE computations (regional annual mean increased up to 0.3 W/m^2). Finally, we note in Table 2 that the peak value of seasonal mean TOA DRE in the North Pacific occurs in the boreal summer (JJA) when the ACA occurrence frequency is low rather than in the spring or winter when there is a larger ACA occurrence frequency. This suggests a stronger role of solar insolation than ACA occurrence frequency.

6. Uncertainty Analysis

In this section, we assess the impact of two major uncertainties on the DRE computation, one associated with the aerosol optical properties and the other associated with the CALIOP AOT retrieval.

6.1. Uncertainty in aerosol optical properties

As indicated in Figure 8, smoke and dust are the two most important types of ACA in terms of DRE. The DRE results in Section 5 are based on the control run, in which smoke and dust aerosols are represented by the CALIOP smoke model in Figure 4a and OBS dust model in Figure 4c. The primary rationale for using the CALIOP smoke model in the control run is that it is consistent with the operational CALIOP retrieval algorithm. As shown in Figure 4a, the CALIOP smoke model has a single scattering albedo ω around 0.85 in the visible region, which is close to the mean value of ω measured during the SAFARI 2000 (Southern African Regional Science Initiative) field campaign (see Figure

692 1 in Leahy et al., 2007). However, it should be noted that most measurements made
693 during the SAFARI 2000 field campaign took place in the southern African continent
694 close to the source of biomass burning aerosols and upstream of the SE Atlantic ACA
695 region. Previous studies have found that the absorption of carbonaceous smoke particles
696 tends to decrease due to the aging effect and mixing with other less absorptive aerosols
697 (Liousse et al., 1993). In order to estimate the impact of aerosol model uncertainty on
698 DRE, we replaced the CALIOP smoke model in our sensitivity tests with the less
699 absorbing aged plume model reported in (Haywood et al., 2003) (referred to as the
700 "Haywood smoke model"). This model is derived from air-borne in situ measurements of
701 aged smoke plumes advected off the coast of Namibia and Angola during the SAFARI
702 2000 campaign. In this model, in situ measured aerosol size distributions are fitted using
703 a summation of three lognormal distributions with two fine modes composed of aged
704 biomass smoke and the third coarse mode composed of mineral dust. The single
705 scattering properties of the Haywood smoke model are shown in Figure 4b. Compared to
706 the CALIOP smoke model, the Haywood smoke model is significantly less absorptive,
707 with a single scattering albedo ω of about 0.90 in the visible region (vs. ω~0.85 for the
708 CALIOP smoke model).

709 To estimate the sensitivity of DRE to dust scattering properties, we developed a new
710 dust scattering model based on the same size distribution as the OBS model but a
711 different spectral refractive index provided in the OPAC database (Hess et al., 1998)
712 (referred to as the "OPAC dust model"). The OPAC dust refractive index has been used
713 for dust optical properties in previous studies by Perlwitz et al. (2001) and Colarco et al.
714 (2010). The single scattering properties of the OPAC dust model are shown in Figure 4d.

With a ω~0.9 in the visible region, OPAC dust is significantly more absorptive than the OBS dust model (ω~0.95 in visible) used in the control run. It should be clarified here that the new models do not necessarily provide a better (or worse) representation of the optical properties of ACA, but their differences from the models used in the control run, especially in terms of aerosol absorption, provide an opportunity to investigate the sensitivity of ACA DRE to the optical properties of ACA.

The results from the sensitivity tests are shown in Figure 14. The annual mean cloudy-sky TOA DRE and DRE efficiency from the control run are shown in Figure 14a and b. In the first sensitivity test, we replaced the CALIOP smoke model with the Haywood smoke model, but kept the OBS dust model. Note that the combination of Haywood smoke and OBS dust are the least absorptive among all possible combinations. As expected the less absorbing Haywood smoke model leads to a significant reduction of positive DRE in the SE Atlantic Ocean (Figure 14c). The annual and seasonal mean of cloudy-sky DRE in this region reduces by a factor of 2 from 0.21 to 0.10 W/m^2. In addition, the DRE efficiency in Figure 14d is also seen to reduce significantly from a regional mean of 9.35 W/m^2/AOT to 3.88 W/m^2/AOT. In the second sensitivity test, we replaced the OBS dust model with the OPAC dust model, but kept the CALIOP smoke model unchanged. Note that the combination of CALIOP smoke and OPAC dust are the most absorptive among all possible combinations. The use of the more absorptive OPAC model reduces the scattering effect of above-cloud dust, which has the most significant impact on the TNE Atlantic region as expected (Figure 14e), reducing the strength of regional annual mean TOA DRE from −0.78 to −0.31 W/m^2. The regional mean DRE efficiency in the region reduces from about −24.2 W/m^2/AOT to −9.5 W/m^2/AOT.

6.2. Uncertainty in CALIOP AOT retrieval

As mentioned in Section 2.1, several previous studies (Jethva et al., 2014; Torres et al., 2013; Waquet et al., 2013b) found that the current operational CALIOP 532nm retrieval algorithm, based on the inversion of the attenuated backscatter profile, often significantly underestimates the AOT, especially for smoke aerosols and during the daytime. This is mainly because the strong attenuation of the upper part of an aerosol layer, plus the small backscatter of aerosol particles, makes the attenuated backscatter signal from the lower part of the layer too low to be detected, which leads to an underestimation of the physical thickness and thereby AOT of the aerosol layer. This issue is more severe for smoke aerosols than dust, due to the small backscatter of smoke aerosols (Liu et al., 2015). A case study of above-cloud smoke by (Jethva et al., 2014) showed that the AOT retrievals from other remote sensing techniques are substantially larger (up to a factor of 5) than the operational CALIOP 532nm retrieval as a result of the abovementioned issue. A recent study by (Liu et al., 2015) estimated that the operational CALIOP nighttime AOT retrieval for smoke aerosol over opaque clouds is underestimated by about 39%. Because of the strong dependence of DRE on AOT, the underestimation of smoke AOT by the operational CALIOP retrieval algorithm would have substantially biased the DRE estimates discussed in Section 5, an effect that was shown previously in (Meyer et al., 2013). A robust quantification of this impact requires either the development and implementation of a new CALIOP retrieval algorithm or the use of an alternate independent data set of multiple year global ACA AOT retrievals, both of which are beyond the scope of this study. Here we attempt to estimate the upper bound of DRE bias due to the underestimate of AOT.

We note that although the CALIOP operational algorithm often misses the real bottom of an ACA layer, most of the time it can detect the top of the cloud beneath. This is because the strong backscatter of cloud droplets makes the attenuated backscatter signal strong enough for the CALIOP feature mask to detect despite the strong attenuation of the overlying ACA layer. Here we assume that the entire layer between the top of the ACA layer ($H_{ACA-top}$) and the cloud top ($H_{cloud-top}$) is occupied by aerosols, and we obtain the AOT for this entire layer by scaling the CALIOP AOT retrieval for ACA as follows:

$$\tau'_{ACA} = \frac{H_{ACA-top} - H_{cloud-top}}{H_{ACA-top} - H^{*}_{ACA-bottom}} \tau_{ACA} \quad , \tag{11}$$

where $H^{*}_{ACA-bottom}$ is the CALIOP retrieved apparent aerosol layer bottom height that is likely biased high. Because the true bottom of the aerosol layer is likely somewhere between the retrieved bottom and cloud top, the scaled AOT τ'_{ACA} is therefore an estimate of the upper limit of the ACA AOT. A comparison of the operational AOT retrievals and the scaled AOT based on Eq. (11) derived from one year of CALIOP data over global ocean is shown in Figure 15. The scaling process systematically shifts the PDFs of AOT to larger values as expected. Globally averaged, the operational CALIOP 532nm AOT for above-cloud smoke (with a mean value of 0.24) is about 43% smaller than the scaled results (mean value about 0.42). This result is encouragingly close to (and larger than) the estimate by Liu et al. (2015) (i.e., 39% underestimation), which seems to suggest that the bottom of the above-cloud smoke layer is much closer to cloud top than the daytime CALIOP observation. The scaling has a similar impact on polluted dust. In contrast, the impact on dust aerosols is smaller. The global mean AOT of above-cloud

783 dust from the operational CALIOP product (mean AOT around 0.31) is about 30%
784 smaller than the scaled result (mean AOT around 0.43). This is also close to the number
785 reported in (Liu et al., 2015) (i.e., 26% underestimation).

786 In the sensitivity test shown Figure 16, we replaced the operational CALIOP
787 532nm retrieval τ_{ACA} with the scaled τ'_{ACA} in the DRE computation. In comparison with
788 the DRE from the control run in Figure 14a, c, and e, the most prominent change is the
789 significant increase of positive TOA DRE in the SE Atlantic region, where ACAs are
790 mostly smoke and polluted dust. For example, assuming the CALIOP smoke model, the
791 regional annual mean TOA DRE increases from about 0.2 W/m^2 if using the operational
792 AOT to more than 0.6 W/m^2 using the scaled AOT (see Table 4). Globally averaged, the
793 annual mean TOA DRE induced by above-cloud smoke increases from about 0.013
794 W/m^2 to 0.035 W/m^2 (see Table 3). Interestingly, the impact on DRE efficiency of AOT
795 scaling is not as strong as the impact on DRE, suggesting that the DRE is generally linear
796 with AOT as also found in previous studies (Meyer et al., 2013; Zhang et al., 2014).

797 In addition to the abovementioned issue, strong background solar noise is another
798 source of uncertainty in the daytime CALIOP aerosol products (Hunt et al., 2009; Liu et
799 al., 2015). To estimate the impact of this uncertainty on our DRE results, we performed
800 another sensitivity test, in which we replaced the daytime CALIOP ACA retrievals,
801 including AOT and aerosol classification, with the nighttime retrievals in our DRE
802 computations. The results are presented in the supplementary material. In summary, we
803 found that CALIOP generally detects more and thicker above-cloud smoke in the
804 nighttime than in the daytime, which has also been noted in previous studies (Meyer et
805 al., 2013). We also noted that CALIOP generally detects less and thinner above-cloud

806 dust in the nighttime than in the daytime. As a result of increased smoke and decreased
807 dust, the annual mean global ocean DRE at TOA are shifted to more positive values,
808 ranging from 0.0 to 0.06 W/m^2 (See Table S1 in supplementary material), compared with
809 the daytime results in Table 4 (−0.03 ~ 0.04 W/m^2). We must emphasize that caution
810 must be taken when interpreting the results from this test. Although solar noise certainly
811 has an important role, other factors, in particular the natural aerosol diurnal cycle, could
812 also cause differences between daytime and nighttime CALIOP aerosol retrievals. Future
813 studies and independent data are needed to better understand these differences.

814 Yet another uncertainty source is the misclassification of aerosol as cloud, or vice
815 versa, by CALIOP. According to Liu et al. (2009), overall the CALIOP cloud and aerosol
816 discrimination algorithm works well in most cases. A 1-day manual verification suggests
817 that the success rate is in the neighborhood of 90% or better. Misclassifications occur
818 mostly in the source regions of dense of dust and smoke. Because this study focused on
819 transported aerosols over ocean, the uncertainty causes by aerosol-cloud misclassification
820 should be negligible in the comparison with other major uncertainties discussed above.

821 ### *6.3. Summary of uncertainty study*

822 Finally, combining the results from the control run (Table 3) and sensitivity tests
823 (Table 4 and Table S2), we estimate that the annual mean diurnally average TOA DRE
824 due to ACA over global ocean is about 0.015 W/m^2 with a range of −0.03 to 0.06 W/m^2.
825 The lower bound (−0.03 W/m^2) is based on the combination of the least absorbing
826 aerosol combination, i.e., Haywood smoke and OBS dust model, and operational (un-
827 scaled) daytime AOT. The upper bound (0.06 W/m^2) is based on the combination of the

most absorbing aerosol models, i.e., CALIOP smoke and OPAC dust model, and scaled nighttime AOT. The DREs at surface and within the atmosphere are −0.15 W/m^2 (with a range of −0.09 to −0.21 W/m^2), and 0.17 W/m^2 (with a range of 0.11 to 0.24 W/m^2), respectively. It should be noted that the rather small TOA DRE when averaged over global ocean is partly because of the cancellation of positive (in SE Atlantic and NW Pacific) and negative (TNE Atlantic and Arabian See) regional DREs. The regional and seasonal mean DREs, as shown in Table 5 and Table S3, could be much stronger. For example, in the SE Atlantic region the JJA seasonal mean cloudy-sky DRE is about 0.7 W/m^2 (with a range of 0.2 to 1.2 W/m^2) at TOA (Table 5 and Table S3). From a different perspective, the results in Table 3 and Table S1 suggest that the light-absorbing ACAs, i.e., smoke and polluted dust, induce an annual mean TOA DRE of about 0.04 W/m^2 (with a range of about 0.015 ~ 0.065 W/m^2), which is largely cancelled by the negative DRE due to above-cloud dust (annual mean of about −0.024 W/m^2 with a range between −0.004 to −0.044 W/m^2).

Overall, we found significant uncertainties in our DRE computation. Even the sign of global ocean mean cloud-sky TOA DRE is uncertain. This is partly because, as analyzed above, the positive DREs in regions dominated by light-absorbing ACAs (i.e., SE Atlantic and NW Pacific) are largely cancelled by the negative DREs in the regions dominated by above-cloud dust (i.e., TNE Atlantic and Arabian Sea). In addition, there are also substantial uncertainties in regional DREs caused by uncertainties in aerosol optical properties, in particular aerosol absorption, and uncertainties in the CALIOP operational aerosol retrieval products. Reducing these uncertainties requires improved knowledge of the optical properties of ACAs, in particular single-scattering albedo, on

851 regional scales, and at the same time more accurate ACA property retrievals, in particular
852 AOT. New measurements from upcoming field campaigns, for example NASA's
853 ORACLES (ObseRvations of Aerosols above CLouds and their intEractionS), will help
854 improve our knowledge of the ACA properties in SE Atlantic region. In addition, the
855 emerging remote sensing techniques summarized in (Yu and Zhang, 2013) will provide
856 independent ACA retrievals to compare and validate the results from this study and
857 improve our understanding of the DRE of ACA. Finally, as pointed out earlier, we have
858 ignored the cloud diurnal cycle in the DRE computation, as well as the uncertainty
859 analysis in this section. The impact of cloud diurnal cycle on DRE computations will be
860 investigated in future work along with updated uncertainty analysis.

861 ## *7. Summary and Discussion*

862 In this study, we used 8 years (2007-2014) of CALIOP ACA and MODIS cloud
863 observations to derive the shortwave DRE of ACA over global oceans. The main findings
864 are summarized below:

865 1) Similar to previous studies, we found high occurrence frequency of ACA in
866 several regions of the globe (see Figure 2), including i) the SE Atlantic where
867 marine boundary layer clouds are persistently covered by smoke and polluted
868 dust aerosols originating from biomass burning activities in the African
869 Savanna; ii) the TNE Atlantic region where ACAs are predominately blown
870 dust from Sahara; iii) the Arabian Sea region where dust aerosols from
871 surrounding deserts overlap with clouds associated with the Asian monsoon;

and iv) the North Pacific region where transported pollution from Asia is often found above clouds in boreal winter and early spring (see Figure 3).

2) In regions where ACAs are dominated by smoke and polluted dust (e.g., SE Atlantic and North Pacific), the cloudy-sky DRE at TOA due to ACA is generally positive, while in regions dominated by dust aerosols (e.g., TNE Atlantic and Arabian Sea) the DRE at TOA is generally negative (see Figure 5). After averaging over global oceans, the light-absorptive ACAs, i.e., smoke and polluted dust, yield a TOA DRE of about 0.04 W/m^2 (range of about 0.015 ~ 0.065 W/m^2). In contrast, above-cloud dusts yield an annual mean of about −0.024 W/m^2 (range of −0.004 to −0.044 W/m^2) (see Table 3). The cancellation of positive and negative DREs results in a rather small global-ocean averaged annual mean cloudy-sky TOA DRE of about 0.015 W/m^2 with a range of −0.03 to 0.06 W/m^2. The global-ocean averaged annual mean cloudy-sky DREs at the surface and within the atmosphere are about −0.15 W/m^2 (range of −0.09 to −0.21 W/m^2), and 0.17 W/m^2 (range of 0.11 to 0.24 W/m^2), respectively.

3) We estimated the impacts on our DRE computation of two major sources of uncertainty, one associated with assumed aerosol optical properties and the other with potential CALIOP AOT retrieval biases. As expected, we found the DRE of ACA is highly sensitive to the aerosol absorption. The use of a less absorptive smoke model can reduce the positive TOA DRE in the SE Atlantic region by a factor of 2 (see Figure 14 and Table 3). The impact of potential low biases in the CALIOP AOT retrieval due to the high bias in the detected

aerosol layer bottom is even stronger. The scaling has a stronger impact on the AOT of smoke than dust (see Figure 15), leading to a less negative or even positive global annual mean DRE. The combination of AOT scaling and using more absorptive aerosol optical models can lead to a global-ocean averaged annual mean TOA DRE of about 0.04 W/m^2 (see Table 4), and up to 0.06 W/m^2 if nighttime CALIOP aerosol retrievals are used.

To our best knowledge, this is the first study to provide an observational-based global and multiyear perspective on the DRE of ACA. Our results can be used for evaluating and improving model simulations of cloudy-sky DRE of aerosols that currently have large diversity (Schulz et al., 2006).

There are several limitations to this study that could be improved in future work. First, as we mentioned in section 4, although we consider the diurnal solar variation we ignored the diurnal variation of cloud and aerosol in our DRE computation. This is because the A-Train observes most regions of the globe only once during the daytime. This is not enough, especially in regions where clouds and/or aerosols have a strong diurnal cycle. For example, as shown in (Min and Zhang, 2014) the cloud fraction in the SE Atlantic region varies substantially from the maximum value of about 80% in the early morning to about 60% in the late afternoon. Cloud liquid water path and cloud optical thickness have a similar diurnal cycle (Wood et al., 2002). Approximating such a strong diurnal cycle using only the snapshot from the afternoon A-train crossing is likely to cause significant errors in DRE computation (Min and Zhang, 2014). In this regard, geostationary observations from, for instance, the SEVIRI (Spinning Enhanced Visible and InfraRed Imager) onboard MSG (MeteoSat Second Generation) (Schmetz et al.,

2002), can be used to assess the impact of cloud diurnal cycle on ACA DRE computation. One of our future work will be using the diurnal cloud observations from SEVIRI and ACA observations from CALIOP or other satellite instruments to study the impact of cloud diurnal cycle on all-sky aerosol forcing in the SE Atlantic region. Second, we used only the aerosol retrievals from CALIOP in DRE computation. As aforementioned, recent studies have found significant biases and uncertainties in the operational CALIOP aerosol product (Jethva et al., 2014; Liu et al., 2015; Meyer et al., 2013). We have tried to estimate the impact of CALIOP retrieval uncertainties on our DRE computations. Nevertheless, future study is needed to better understand the uncertainties in our results. The emerging ACA property retrievals from the passive satellite sensors would provide independent datasets for such studies (Jethva et al., 2013; Meyer et al., 2015; Torres et al., 2011; Waquet et al., 2009). Finally, our current knowledge on the microphysical and optical properties of ACAs is still very limited due to the lack of measurements in comparison with clear-sky aerosols (e.g., no measurement from AERONET). New measurements from upcoming field campaigns, for example NASA's ORACLES (ObseRvations of Aerosols above CLouds and their intEractionS), and emerging satellite remote sensing techniques will help improve our DRE computations in the future.

Acknowledgement:

Z. Zhang is supported by NASA grant NNX14AI35G managed by Dr. Ming-Ying Wei. K. Meyer acknowledges support by the NASA Radiation Sciences Program, and by funding from NASA CloudSat and CALIPSO Science Team grant (NNH14CK44C) managed by Dr. David Considine. H. Yu was supported by the NASA CALIPSO/CloudSat project (NNX14AB21G) managed by Dr. David Considine. The computations in this study were performed on UMBC High Performance Computing Facility (HPCF). The facility is supported by the U.S. National Science Foundation through the MRI program (grant nos. CNS-0821258 and CNS-1228778) and the SCREMS program (grant no. DMS-0821311), with additional substantial support from UMBC.

949

950 **References**:

951 Abel, S. J., Highwood, E. J., Haywood, J. M. and Stringer, M. A.: The direct radiative
952 effect of biomass burning aerosols over southern Africa, Atmospheric Chemistry and
953 Physics, 5(7), 1999–2018, doi:10.5194/acp-5-1999-2005, 2005.

954 Ackerman, S., Strabala, K., Menzel, W., Frey, R., Moeller, C. and Gumley, L.:
955 Discriminating clear sky from clouds with MODIS, Journal of Geophysical Research,
956 103(D24), 32,141–32,157, 1998.

957 Baum, B. A., Menzel, W. P., Frey, R. A., Tobin, D. C., Holz, R. E., Ackerman, S. A.,
958 Heidinger, A. K. and Yang, P.: MODIS Cloud-Top Property Refinements for Collection
959 6, J. Appl. Meteor. Climatol., 51(6), 1145–1163, doi:10.1175/JAMC-D-11-0203.1, 2012.

960 Burton, S. P., Ferrare, R. A., Vaughan, M. A., Omar, A. H., Rogers, R. R., Hostetler, C.
961 A. and Hair, J. W.: Aerosol classification from airborne HSRL and comparisons with the
962 CALIPSO vertical feature mask, Atmos. Meas. Tech., 6(5), 1397–1412, doi:10.5194/amt-
963 6-1397-2013, 2013.

964 Chand, D., Anderson, T. L., Wood, R., Charlson, R. J., Hu, Y., Liu, Z. and Vaughan, M.:
965 Quantifying above‐cloud aerosol using spaceborne lidar for improved understanding of
966 cloudy‐sky direct climate forcing, J. Geophys. Res., 113(D13), D13206,
967 doi:10.1029/2007JD009433, 2008.

968 Chand, D., Wood, R., Anderson, T. L., Satheesh, S. K. and Charlson, R. J.: Satellite-
969 derived direct radiative effect of aerosols dependent on cloud cover, Nature Geoscience,
970 2(3), 181–184, doi:10.1038/ngeo437, 2009.

971 Clough, S. A., Shephard, M. W., Mlawer, E. J., Delamere, J. S., Iacono, M. J., Cady-
972 Pereira, K., Boukabara, S. and Brown, P. D.: Atmospheric radiative transfer modeling: a
973 summary of the AER codes, Journal of Quantitative Spectroscopy and Radiative Transfer
974 VL -, 91(2), 233–244, 2005.

975 Coddington, O. M., Pilewskie, P., Redemann, J., Platnick, S., Russell, P. B., Schmidt, K.
976 S., Gore, W. J., Livingston, J., Wind, G. and Vukicevic, T.: Examining the impact of
977 overlying aerosols on the retrieval of cloud optical properties from passive remote
978 sensing, J. Geophys. Res., 115(D10), D10211, doi:10.1029/2009JD012829, 2010.

979 Colarco, P. R., Nowottnick, E. P., Randles, C. A., Yi, B., Yang, P., Kim, K. M., Smith, J.
980 A. and Bardeen, C. G.: Impact of radiatively interactive dust aerosols in the NASA
981 GEOS‐5 climate model: Sensitivity to dust particle shape and refractive index, Journal of
982 Geophysical Research-Atmospheres, 119(2), 753–786, doi:10.1002/2013JD020046,
983 2014.

Colarco, P. R., Toon, O. B., Torres, O. and Rasch, P. J.: Determining the UV imaginary index of refraction of Saharan dust particles from Total Ozone Mapping Spectrometer data using a three-dimensional model of dust transport, J. Geophys. Res., 107(D16), AAC 4–1–AAC 4–18, doi:10.1029/2001JD000903, 2002.

Colarco, P., da Silva, A., Chin, M. and Diehl, T.: Online simulations of global aerosol distributions in the NASA GEOS-4 model and comparisons to satellite and ground-based aerosol optical depth, J. Geophys. Res., 115(D14), D14207, doi:10.1029/2009JD012820, 2010.

de Graaf, M., Bellouin, N., Tilstra, L. G., Haywood, J. and Stammes, P.: Aerosol direct radiative effect of smoke over clouds over the southeast Atlantic Ocean from 2006 to 2009, Geophysical Research Letters, 41(21), 7723–7730, doi:10.1002/2014GL061103, 2014.

de Graaf, M., Tilstra, L. G., Wang, P. and Stammes, P.: Retrieval of the aerosol direct radiative effect over clouds from spaceborne spectrometry, J. Geophys. Res., 117(D7), D07207–n/a, doi:10.1029/2011JD017160, 2012.

Devasthale, A. and Thomas, M. A.: A global survey of aerosol-liquid water cloud overlap based on four years of CALIPSO-CALIOP data, Atmospheric Chemistry and Physics, 11(3), 1143–1154, doi:10.5194/acp-11-1143-2011, 2011.

Eck, T. F., Holben, B. N., Reid, J. S., Mukelabai, M. M., Piketh, S. J., Torres, O., Jethva, H. T., Hyer, E. J., Ward, D. E., Dubovik, O., Sinyuk, A., Schafer, J. S., Giles, D. M., Sorokin, M., Smirnov, A. and Slutsker, I.: A seasonal trend of single scattering albedo in southern African biomass-burning particles: Implications for satellite products and estimates of emissions for the world's largest biomass-burning source, Journal of Geophysical Research-Atmospheres, 118(12), 6414–6432, doi:10.1002/jgrd.50500, 2013.

Feng, N. and Christopher, S. A.: Measurement-based estimates of direct radiative effects of absorbing aerosols above clouds, Journal of Geophysical Research-Atmospheres, 120(14), 2015JD023252–n/a, doi:10.1002/2015JD023252, 2015.

Haywood, J. M., Osborne, S. R. and Abel, S. J.: The effect of overlying absorbing aerosol layers on remote sensing retrievals of cloud effective radius and cloud optical depth, Quarterly Journal of the Royal Meteorological Society, 130(598), 779–800, doi:10.1256/qj.03.100, 2004.

Haywood, J. M., Osborne, S. R., Francis, P. N., Keil, A., Formenti, P., Andreae, M. O. and Kaye, P. H.: The mean physical and optical properties of regional haze dominated by biomass burning aerosol measured from the C-130 aircraft during SAFARI 2000, J. Geophys. Res., 108(D13), 8473, doi:10.1029/2002JD002226, 2003.

Hess, M., Koepke, P. and Schult, I.: Optical Properties of Aerosols and Clouds: The Software Package OPAC, Bull. Amer. Meteor. Soc., 79(5), 831–844, doi:10.1175/1520-

0477(1998)079<0831:OPOAAC>2.0.CO;2, 1998.

Hu, Y., Vaughan, M., Liu, Z., Lin, B., Yang, P., Flittner, D., Hunt, B., Kuehn, R., Huang, J., Wu, D., Rodier, S., Powell, K., Trepte, C. and Winker, D.: The depolarization - attenuated backscatter relation: CALIPSO lidar measurements vs. theory, Opt. Express, 15(9), 5327–5332, doi:10.1364/OE.15.005327, 2007.

Hubanks, P. A., King, M. D., Platnick, S. and Pincus, R.: MODIS atmosphere L3 gridded product algorithm theoretical basis document, Algorithm Theor. Basis Doc. ATBD-MOD, 30, 2008.

Hunt, W. H., Winker, D. M., Vaughan, M. A., Powell, K. A., Lucker, P. L. and Weimer, C.: CALIPSO Lidar Description and Performance Assessment, J. Atmos. Oceanic Technol., 26(7), 1214–1228, doi:10.1175/2009JTECHA1223.1, 2009.

Iacono, M. J., Delamere, J. S., Mlawer, E. J., Shephard, M. W., Clough, S. A. and Collins, W. D.: Radiative forcing by long-lived greenhouse gases: Calculations with the AER radiative transfer models, J. Geophys. Res., 113(D13), D13103, doi:10.1029/2008JD009944, 2008.

Ichoku, C., Remer, L. A., Kaufman, Y. J., Levy, R., Chu, D. A., Tanré, D. and Holben, B. N.: MODIS observation of aerosols and estimation of aerosol radiative forcing over southern Africa during SAFARI 2000, J. Geophys. Res., 108(D13), 8499, doi:10.1029/2002JD002366, 2003.

Jethva, H., Torres, O., Remer, L. A. and Bhartia, P. K.: A color ratio method for simultaneous retrieval of aerosol and cloud optical thickness of above-cloud absorbing aerosols from passive sensors: Application to MODIS measurements, IEEE TRANSACTIONS ON GEOSCIENCE AND REMOTE SENSING, 51(7), 3862–3870, 2013.

Jethva, H., Torres, O., Waquet, F., Chand, D. and Hu, Y.: How do A-train sensors intercompare in the retrieval of above-cloud aerosol optical depth? A case study-based assessment, Geophysical Research Letters, 41(1), 186–192, doi:10.1002/2013GL058405, 2014.

Keil, A. and Haywood, J. M.: Solar radiative forcing by biomass burning aerosol particles during SAFARI 2000: A case study based on measured aerosol and cloud properties, J Geophys Res, 108(D13), 8467, doi:10.1029/2002JD002315, 2003.

Kim, D., Chin, M., Yu, H., Eck, T. F., Sinyuk, A., Smirnov, A. and Holben, B. N.: Dust optical properties over North Africa and Arabian Peninsula derived from the AERONET dataset, Atmospheric Chemistry and Physics, 11(20), 10733–10741, doi:10.5194/acp-11-10733-2011, 2011.

Leahy, L. V., Anderson, T. L., Eck, T. F. and Bergstrom, R. W.: A synthesis of single scattering albedo of biomass burning aerosol over southern Africa during SAFARI 2000,

1058 Geophysical Research Letters, 34(12), L12814, doi:10.1029/2007GL029697, 2007.

1059 Liousse, C., Cachier, H. and Jennings, S. G.: Optical and thermal measurements of black
1060 carbon aerosol content in different environments: Variation of the specific attenuation
1061 cross-section, sigma (σ), Atmospheric Environment. Part A. General Topics, 27(8),
1062 1203–1211, doi:10.1016/0960-1686(93)90246-U, 1993.

1063 Liu, Z., Vaughan, M., Winker, D., Kittaka, C., Getzewich, B., Kuehn, R., Omar, A.,
1064 Powell, K., Trepte, C. and Hostetler, C.: The CALIPSOLidar Cloud and Aerosol
1065 Discrimination: Version 2 Algorithm and Initial Assessment of Performance, Journal of
1066 Atmospheric and Oceanic Technology, 26(7), 1198–1213,
1067 doi:10.1175/2009JTECHA1229.1, 2009.

1068 Liu, Z., Winker, D., Omar, A., Vaughan, M., Kar, J., Trepte, C., Hu, Y. and Schuster, G.:
1069 Evaluation of CALIOP 532 nm aerosol optical depth over opaque water clouds, ACP,
1070 15(3), 1265–1288, doi:10.5194/acpd-14-23583-2014, 2015.

1071 Marchant, B., Platnick, S., Meyer, K. G., Arnold, G. T. and Riedi, J.: MODIS Collection
1072 6 shortwave-derived cloud phase classification algorithm and comparisons with CALIOP,
1073 Atmospheric Chemistry and Physics, Submitted, 2015.

1074 Matichuk, R. I., Colarco, P. R., Smith, J. A. and Toon, O. B.: Modeling the transport and
1075 optical properties of smoke aerosols from African savanna fires during the Southern
1076 African Regional Science Initiative campaign (SAFARI 2000), J. Geophys. Res.,
1077 112(D8), D08203, doi:10.1029/2006JD007528, 2007.

1078 Menzel, P., Frey, R., Baum, B. and Zhang, H.: Cloud Top Properties and Cloud Phase
1079 Algorithm Theoretical Basis Document. 2006.

1080 Menzel, W., Smith, W. and Stewart, T.: Improved Cloud Motion Wind Vector and
1081 Altitude Assignment Using VAS, Journal of Applied Meteorology, 22(3), 377–384,
1082 1983.

1083 Meyer, K., Platnick, S. and Zhang, Z.: Simultaneously inferring above‐cloud absorbing
1084 aerosol optical thickness and underlying liquid phase cloud optical and microphysical
1085 properties using MODIS, Journal of Geophysical Research-Atmospheres, 120(11), 5524–
1086 5547, doi:10.1002/2015JD023128, 2015.

1087 Meyer, K., Platnick, S., Oreopoulos, L. and Lee, D.: Estimating the direct radiative effect
1088 of absorbing aerosols overlying marine boundary layer clouds in the southeast Atlantic
1089 using MODIS and CALIOP, Journal of Geophysical Research-Atmospheres, 118(10),
1090 4801–4815, doi:10.1002/jgrd.50449, 2013.

1091 Min, M. and Zhang, Z.: On the influence of cloud fraction diurnal cycle and sub-grid
1092 cloud optical thickness variability on all-sky direct aerosol radiative forcing, Journal of
1093 Quantitative Spectroscopy and Radiative Transfer, 142 IS -, 25–36,
1094 doi:10.1016/j.jqsrt.2014.03.014, 2014.

1095 Myhre, G., Berntsen, T. K., Haywood, J. M., Sundet, J. K., Holben, B. N., Johnsrud, M.
1096 and Stordal, F.: Modeling the solar radiative impact of aerosols from biomass burning
1097 during the Southern African Regional Science Initiative (SAFARI-2000) experiment, J.
1098 Geophys. Res., 108(D13), 8501, doi:10.1029/2002JD002313, 2003.

1099 Nakajima, T. and King, M. D.: Determination of the Optical Thickness and Effective
1100 Particle Radius of Clouds from Reflected Solar Radiation Measurements. Part I: Theory,
1101 J. Atmos. Sci., 47(15), 1878–1893, doi:10.1175/1520-
1102 0469(1990)047<1878:DOTOTA>2.0.CO;2, 1990.

1103 Nowottnick, E. P., Colarco, P. R., Welton, E. J. and da Silva, A.: Use of the CALIOP
1104 vertical feature mask for evaluating global aerosol models, Atmos. Meas. Tech. Discuss.,
1105 8(1), 1401–1455, doi:10.5194/amtd-8-1401-2015, 2015.

1106 Omar, A. H., Winker, D. M., Vaughan, M. A., Hu, Y., Trepte, C. R., Ferrare, R. A., Lee,
1107 K.-P., Hostetler, C. A., Kittaka, C. and Rogers, R. R.: The CALIPSO automated aerosol
1108 classification and lidar ratio selection algorithm, Journal of Atmospheric and Oceanic
1109 Technology, 26(10), 1994–2014, 2009.

1110 Perlwitz, J., Tegen, I. and Miller, R. L.: Interactive soil dust aerosol model in the GISS
1111 GCM: 1. Sensitivity of the soil dust cycle to radiative properties of soil dust aerosols, J.
1112 Geophys. Res., 106(D16), 18167–18192, doi:10.1029/2000JD900668, 2001.

1113 Peters, K., Quaas, J. and Bellouin, N.: Effects of absorbing aerosols in cloudy skies: a
1114 satellite study over the Atlantic Ocean, Atmos. Chem. Phys, 11, 1393–1404, 2011.

1115 Platnick, S., King, M. D., Ackerman, S. A., Menzel, W. P., Baum, B. A., Riédi, J. C. and
1116 Frey, R. A.: The MODIS cloud products: algorithms and examples from Terra, IEEE
1117 TRANSACTIONS ON GEOSCIENCE AND REMOTE SENSING, 41(2), 459–473,
1118 doi:10.1109/TGRS.2002.808301, 2003.

1119 Schmetz, J., Pili, P., Tjemkes, S., Just, D., Kerkmann, J., Rota, S. and Ratier, A.: An
1120 Introduction to Meteosat Second Generation (MSG), Bull. Amer. Meteor. Soc., 83(7),
1121 977–992, doi:10.1175/1520-0477(2002)083<0977:AITMSG>2.3.CO;2, 2002.

1122 Schulz, M., Textor, C., Kinne, S., Balkanski, Y., Bauer, S., Berntsen, T., Berglen, T.,
1123 Boucher, O., Dentener, F., Guibert, S., Isaksen, I. S. A., Iversen, T., Koch, D., Kirkevåg,
1124 A., Liu, X., Montanaro, V., Myhre, G., Penner, J. E., Pitari, G., Reddy, S., Seland, Ø.,
1125 Stier, P. and Takemura, T.: Radiative forcing by aerosols as derived from the AeroCom
1126 present-day and pre-industrial simulations, Atmos. Chem. Phys, 6, 5225–5246, 2006.

1127 Shettle, E. P. and Fenn, R. W.: Models for the Aerosols of the Lower Atmosphere and the
1128 Effects of Humidity Variations on their Optical Properties,, 1979.

1129 Stephens, G. L., Vane, D. G., Boain, R. J., Mace, G. G., Sassen, K., Wang, Z.,
1130 Illingworth, A. J., O'Connor, E. J., Rossow, W. B., Durden, S. L., Miller, S. D., Austin,
1131 R. T., Benedetti, A., Mitrescu, C. and CloudSat Science Team, T.: THE CLOUDSAT
1132 MISSION AND THE A-TRAIN,, 83(12), 1771–1790, doi:10.1175/BAMS-83-12-1771,

2002.

Swap, R., Garstang, M., Macko, S. A., Tyson, P. D., Maenhaut, W., Artaxo, P., Kållberg, P. and Talbot, R.: The long-range transport of southern African aerosols to the tropical South Atlantic, J. Geophys. Res., 101(D19), 23777–23791, doi:10.1029/95JD01049, 1996.

Torres, O., Ahn, C. and Chen, Z.: Improvements to the OMI near-UV aerosol algorithm using A-train CALIOP and AIRS observations, Atmos. Meas. Tech., 6(11), 3257–3270, doi:10.5194/amt-6-3257-2013, 2013.

Torres, O., Jethva, H. and Bhartia, P. K.: Retrieval of Aerosol Optical Depth above Clouds from OMI Observations: Sensitivity Analysis and Case Studies, J. Atmos. Sci., 69(3), 1037–1053, doi:10.1175/JAS-D-11-0130.1, 2011.

Waquet, F., Cornet, C., Deuzé, J. L., Dubovik, O., Ducos, F., Goloub, P., Herman, M., Lapyonok, T., C Labonnote, L., Riedi, J., Tanre, D., Thieuleux, F. and Vanbauce, C.: Retrieval of aerosol microphysical and optical properties above liquid clouds from POLDER/PARASOL polarization measurements, Atmos. Meas. Tech., 6(4), 991–1016, doi:10.5194/amt-6-991-2013, 2013a.

Waquet, F., Peers, F., Ducos, F., Goloub, P., Platnick, S., Riedi, J., Tanre, D. and Thieuleux, F.: Global analysis of aerosol properties above clouds, Geophys Res Lett, 40(21), 5809–5814, doi:10.1002/2013GL057482, 2013b.

Waquet, F., Riedi, J., C Labonnote, L., Goloub, P., Cairns, B., Deuzé, J. L. and Tanre, D.: Aerosol Remote Sensing over Clouds Using A-Train Observations, J. Atmos. Sci., 66(8), 2468–2480, doi:10.1175/2009JAS3026.1, 2009.

Wilcox, E. M.: Direct and semi-direct radiative forcing of smoke aerosols over clouds, Atmospheric Chemistry and Physics, 12(1), 139–149, doi:10.5194/acp-12-139-2012, 2012.

Winker, D. M., Hunt, W. H. and McGill, M. J.: Initial performance assessment of CALIOP, Geophysical Research Letters, 34(19), L19803, doi:10.1029/2007GL030135, 2007.

Winker, D. M., Tackett, J. L., Getzewich, B. J., Liu, Z., Vaughan, M. A. and Rogers, R. R.: The global 3-D distribution of tropospheric aerosols as characterized by CALIOP, ACP, 13(6), 3345–3361, doi:10.5194/acp-13-3345-2013, 2013.

Winker, D. M., Vaughan, M. A., Omar, A., Hu, Y., Powell, K. A., Liu, Z., Hunt, W. H. and Young, S. A.: Overview of the CALIPSO mission and CALIOP data processing algorithms, Journal of Atmospheric and Oceanic Technology, 26(11), 2310–2323, 2009.

Wiscombe, W.: Improved Mie scattering algorithms, Appl. Opt, 19(9), 1505–1509, 1980.

Wood, R., Bretherton, C. S. and Hartmann, D. L.: Diurnal cycle of liquid water path over

1169 the subtropical and tropical oceans, Geophysical Research Letters, 29(23), 7–1–7–4,
1170 doi:10.1029/2002GL015371, 2002.

1171 Young, S. A. and Vaughan, M. A.: The Retrieval of Profiles of Particulate Extinction
1172 from Cloud-Aerosol Lidar Infrared Pathfinder Satellite Observations (CALIPSO) Data:
1173 Algorithm Description, J. Atmos. Oceanic Technol., 26(6), 1105–1119, doi:doi:
1174 10.1175/2008JTECHA1221.1, 2008.

1175 Yu, H. and Zhang, Z.: New Directions: Emerging satellite observations of above-cloud
1176 aerosols and direct radiative forcing, Atmospheric Environment, 72(0), 36–40,
1177 doi:10.1016/j.atmosenv.2013.02.017, 2013.

1178 Yu, H., Kaufman, Y. J., Chin, M., Feingold, G., Remer, L. A., Anderson, T. L.,
1179 Balkanski, Y., Bellouin, N., Boucher, O. and Christopher, S.: A review of measurement-
1180 based assessments of the aerosol direct radiative effect and forcing, Atmospheric
1181 Chemistry and Physics, 6(3), 613–666, 2006.

1182 Yu, H., Zhang, Y., Chin, M., Liu, Z., Omar, A., Remer, L. A., Yang, Y., Yuan, T. and
1183 Zhang, J.: An integrated analysis of aerosol above clouds from A-Train multi-sensor
1184 measurements, Remote Sensing of Environment, 121, 125–131,
1185 doi:10.1016/j.rse.2012.01.011, 2010.

1186 Zhang, Z., Meyer, K., Platnick, S., Oreopoulos, L., Lee, D. and Yu, H.: A novel method
1187 for estimating shortwave direct radiative effect of above-cloud aerosols using CALIOP
1188 and MODIS data, Atmos. Meas. Tech., 7(6), 1777–1789, doi:10.5194/amt-7-1777-2014,
1189 2014.

1190

1191

1192 Tables:

1193 Table 1 Geo-locations of four active ACA regions.

Region	Latitude and longitude region
Southeastern Atlantic	30°S~10°N; 20°W~20°E
Tropical Northeastern Atlantic	10°N~30°N; 45°W~18°W
Arabian Sea	0°~30°N; 40°E~80°E
Northwestern Pacific	40°N~55°N; 145°E~180°E

1194

1195

Table 2 The seasonal and annual mean of diurnally averaged cloudy-sky DREs due to ACA at TOA (numbers on the top in each cell), surface (numbers in the middle) and within atmosphere (numbers on bottom). The unit is W/m^2.

Region	DRE	DJF	MAM	JJA	SON	Annual
SE Atlantic Ocean	DRE_{TOA}	−0.02	−0.04	0.41	0.44	0.21
	DRE_{SFC}	−0.21	−0.15	−0.56	−0.49	−0.34
	DRE_{ATM}	0.19	0.11	0.98	0.93	0.56
TNE Atlantic Ocean	DRE_{TOA}	−0.05	−0.57	−2.39	−0.20	−0.78
	DRE_{SFC}	−0.21	−1.45	−5.99	−0.48	−1.99
	DRE_{ATM}	0.16	0.88	3.60	0.28	1.21
Arabian Sea	DRE_{TOA}	−0.02	−0.44	−0.97	−0.25	−0.54
	DRE_{SFC}	−0.16	−1.11	−2.44	−0.73	−1.41
	DRE_{ATM}	0.14	0.67	1.47	0.48	0.88
NWPacific Ocean	DRE_{TOA}	0.01	0.05	0.08	0.01	0.04
	DRE_{SFC}	−0.03	−0.07	−0.07	−0.01	−0.05
	DRE_{ATM}	0.04	0.12	0.15	0.03	0.09
Global Ocean	DRE_{TOA}	0.00	−0.02	−0.06	0.01	−0.02
	DRE_{SFC}	−0.04	−0.11	−0.27	−0.07	−0.13
	DRE_{ATM}	0.04	0.09	0.20	0.08	0.11

Table 3 The global annual mean of diurnally averaged cloudy-sky DREs at TOA induced by different types of ACA according to CALIOP observations. The numbers in the parentheses are results based on the scaled AOT (See section 6.2 for details). The unit is W/m^2.

Type		CALIOP smoke+OBS dust	Haywood smoke+OBS dust	CALIOP smoke+OPAC dust
Smoke	DRE_{TOA}	0.013 (0.035)	0.005 (0.018)	0.013 (0.035)
	DRE_{SFC}	−0.011 (−0.025)	−0.021 (−0.052)	−0.011 (−0.025)
	DRE_{ATM}	0.023 (0.060)	0.026 (0.070)	0.023 (0.060)
Dust	DRE_{TOA}	−0.036 (−0.044)	−0.036 (−0.044)	−0.014 (−0.014)
	DRE_{SFC}	−0.088 (−0.116)	−0.088 (−0.116)	−0.106 (−0.141)
	DRE_{ATM}	0.051 (0.071)	0.051 (0.071)	0.092 (0.127)
Polluted Dust	DRE_{TOA}	0.009 (0.019)	0.009 (0.019)	0.009 (0.019)
	DRE_{SFC}	−0.021 (−0.035)	−0.021 (−0.035)	−0.021 (−0.035)
	DRE_{ATM}	0.030 (0.054)	0.030 (0.054)	0.030 (0.054)

Table 4 The regional and annual mean of diurnally averaged cloudy-sky DREs at TOA based on different combinations of aerosol optical models. The numbers in the parentheses are results based on the scaled AOT (See section 6.2 for details). The unit is W/m^2.

Region		CALIOP smoke+OBS dust	Haywood smoke+OBS dust	CALIOP smoke+OPAC dust
SE Atlantic	DRE_{TOA}	0.21 (0.67)	0.10 (0.38)	0.23 (0.68)
	DRE_{SFC}	−0.34 (−0.73)	−0.50 (−1.13)	−0.36 (−0.76)
	DRE_{ATM}	0.56 (1.37)	0.59 (1.51)	0.60 (1.44)
TNE Atlantic	DRE_{TOA}	−0.78 (−1.00)	−0.78 (−0.99)	−0.31 (−0.34)
	DRE_{SFC}	−1.99 (−2.68)	−1.99 (−2.67)	−2.40 (−3.22)
	DRE_{ATM}	1.22 (1.69)	1.21 (1.70)	2.09 (2.88)
Arabian Sea	DRE_{TOA}	−0.54 (−0.59)	−0.54 (−0.59)	−0.25 (−0.27)
	DRE_{SFC}	−1.41 (−1.59)	−1.42 (−1.60)	−1.67 (−1.88)
	DRE_{ATM}	0.88 (1.00)	0.88 (1.00)	1.42 (1.62)
NW Pacific	DRE_{TOA}	0.04 (0.12)	0.04 (0.10)	0.05 (0.14)
	DRE_{SFC}	−0.05 (−0.12)	−0.06 (−0.16)	−0.05 (−0.13)
	DRE_{ATM}	0.09 (0.24)	0.1 (0.26)	0.10 (0.27)
Global Ocean	DRE_{TOA}	−0.02 (0.00)	−0.03 (−0.01)	0.00 (0.04)
	DRE_{SFC}	−0.13 (−0.18)	−0.14 (−0.21)	−0.14 (−0.20)
	DRE_{ATM}	0.11 (0.18)	0.11 (0.20)	0.14 (0.24)

Table 5 Same as Table 4, except for JJA seasonal mean.

Region		CALIOP smoke+OBS dust	Haywood smoke+OBS dust	CALIOP smoke+OPAC dust
SE Atlantic	DRE_{TOA}	0.41 (1.12)	0.21 (0.67)	0.44 (1.17)
	DRE_{SFC}	−0.56 (1.20)	−0.85 (−1.89)	−0.58 (−1.22)
	DRE_{ATM}	0.98 (2.32)	1.06 (2.57)	1.01 (2.40)
TNE Atlantic	DRE_{TOA}	−2.39 (−3.05)	−2.39 (−3.06)	−0.91 (−1.03)
	DRE_{SFC}	−5.99 (−8.10)	−5.99 (−8.10)	−7.26 (−9.80)
	DRE_{ATM}	3.60 (5.04)	3.60 (5.04)	6.35 (8.77)
Arabian Sea	DRE_{TOA}	−0.97 (−1.06)	−0.97 (−1.07)	−0.46 (−0.49)
	DRE_{SFC}	−2.44 (−2.76)	−2.44 (−2.76)	−2.92 (−3.30)
	DRE_{ATM}	1.47 (1.70)	1.47 (1.70)	2.46 (2.81)
NW Pacific	DRE_{TOA}	0.08 (0.22)	0.06 (0.19)	0.09 (0.24)
	DRE_{SFC}	−0.07 (−0.20)	−0.10 (−0.27)	−0.08 (−0.20)
	DRE_{ATM}	0.15 (0.41)	0.16 (0.46)	0.17 (0.44)
Global Ocean	DRE_{TOA}	−0.06 (−0.04)	−0.08 (−0.06)	0.00 (0.03)
	DRE_{SFC}	−0.27 (−0.38)	−0.28 (−0.42)	−0.31 (−0.44)
	DRE_{ATM}	0.20 (0.34)	0.21 (0.36)	0.31 (0.47)

Figures:

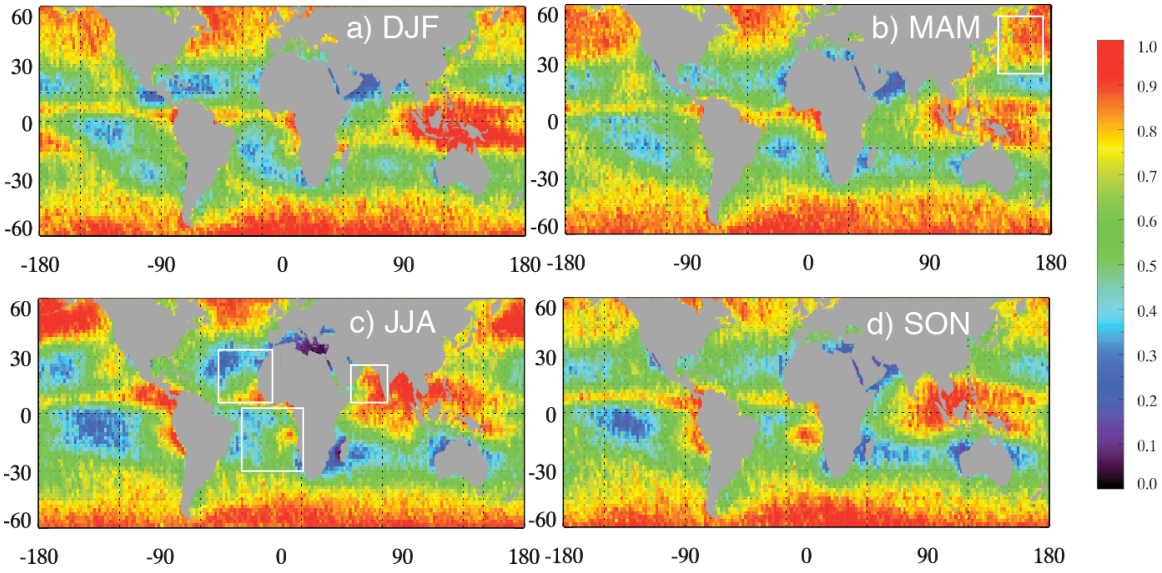

Figure 1 Multiyear seasonal mean total cloud fraction in a) DJF, b) MAM, c) JJA and d) SON derived from 8 years of daytime CALIOP observations.

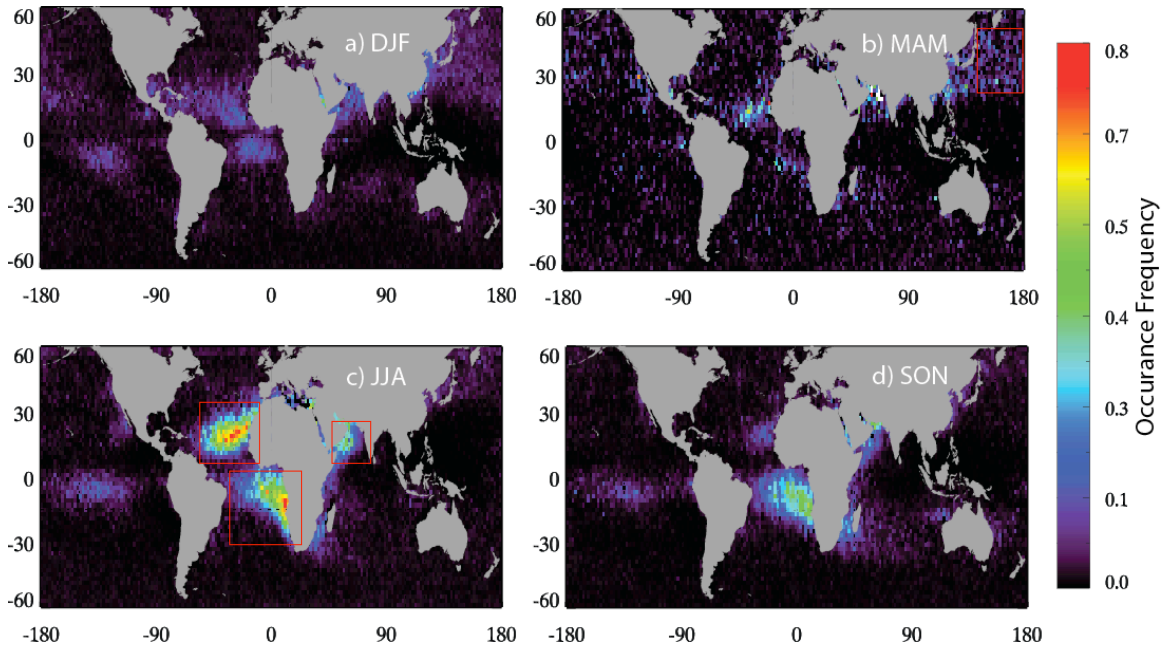

1229

1230 Figure 2 Multiyear seasonal mean occurrence frequency of ACA (f_{ACA}) in a) DJF, b)
1231 MAM, c) JJA and d) SON derived from 8 years of daytime CALIOP observations. The
1232 red boxes indicate the 4 regions with high ACA occurrence frequency. See also Table 1
1233 for the exact geolocation.

1234

1235

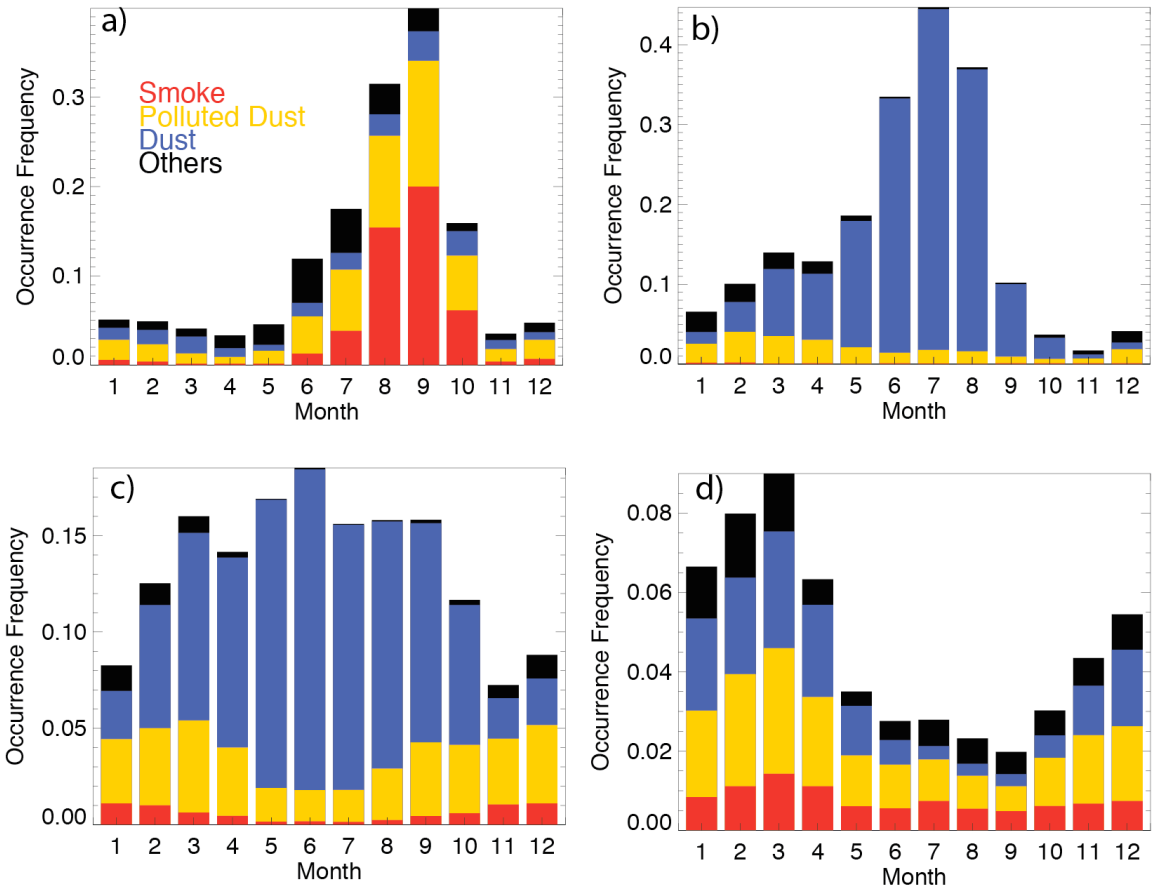

1236

1237 Figure 3 8-year averaged monthly mean daytime occurrence frequency of aerosol types
1238 observed by CALIOP for the a) Southeast Atlantic region, b) North tropical Atlantic
1239 region, c) Arabian Sea, and d) Northwestern Pacific.

1240

1241

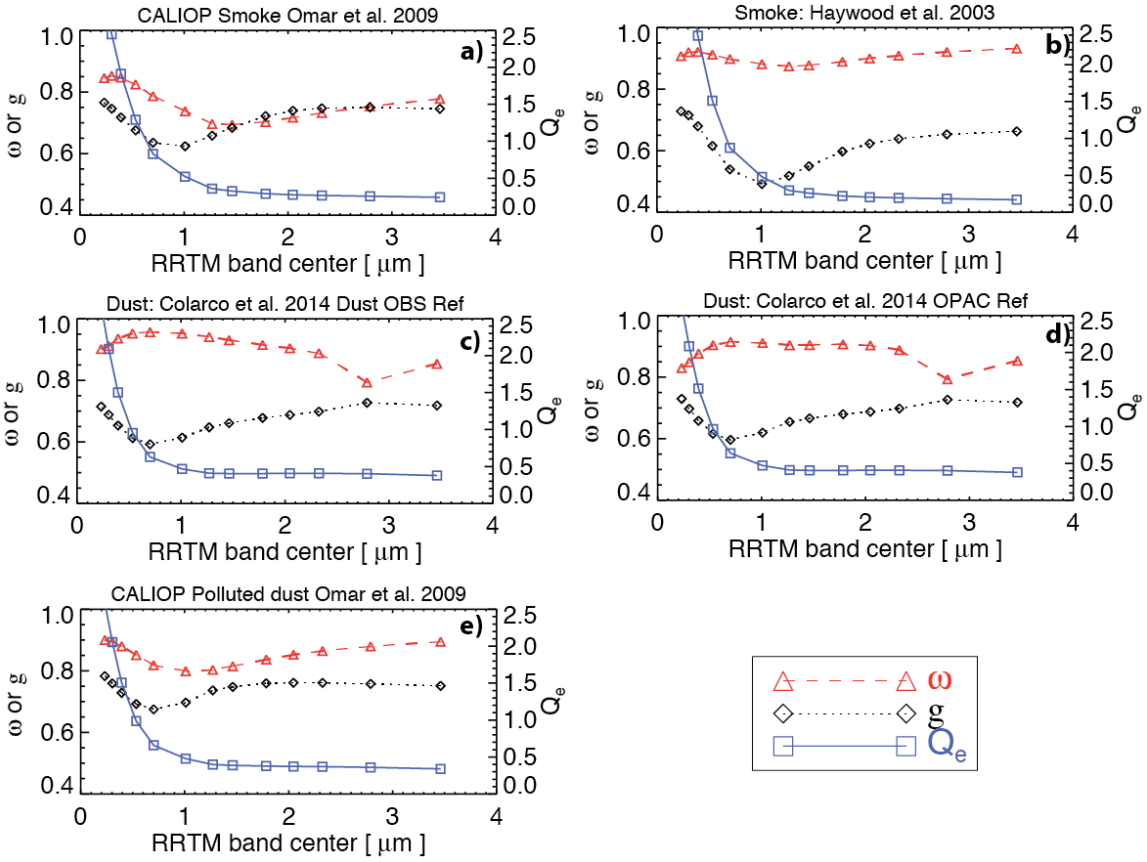

1242

1243 Figure 4 Single scattering properties, including extinction efficiency (Qe), single-
1244 scattering albedo (ω), and asymmetry factor (g) for a) CALIOP smoke, b) Haywood
1245 smoke, c) OBS dust, d) OPAC dust, and e) CALIOP polluted dust.

1246

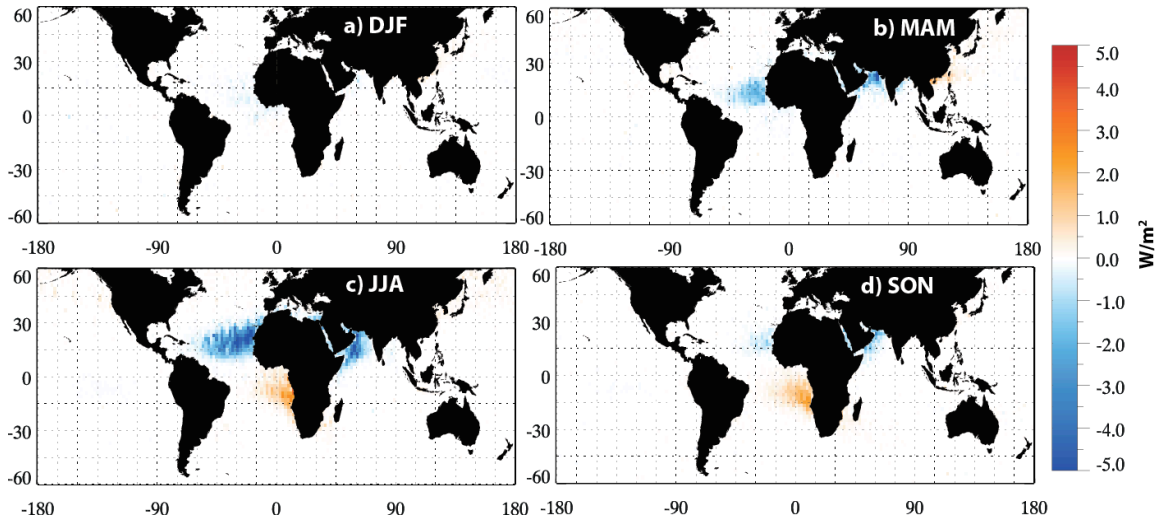

Figure 5: 8-year seasonal mean diurnally averaged shortwave cloudy-sky DRE at TOA, using the CALIOP smoke and OBS dust aerosol models. The ACA AOT in the computation is from the CALIOP operational product without any adjustment.

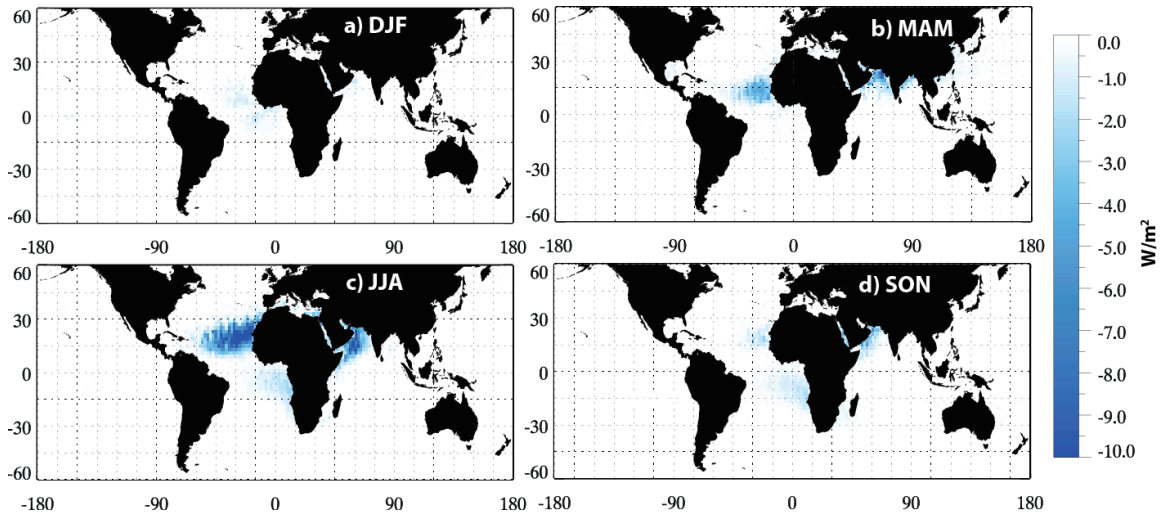

Figure 6 8-year seasonal mean diurnally averaged shortwave cloudy-sky DRE at surface, using the CALIOP smoke and OBS dust aerosol models. The ACA AOT in the computation is from the CALIOP operational product without any adjustment.

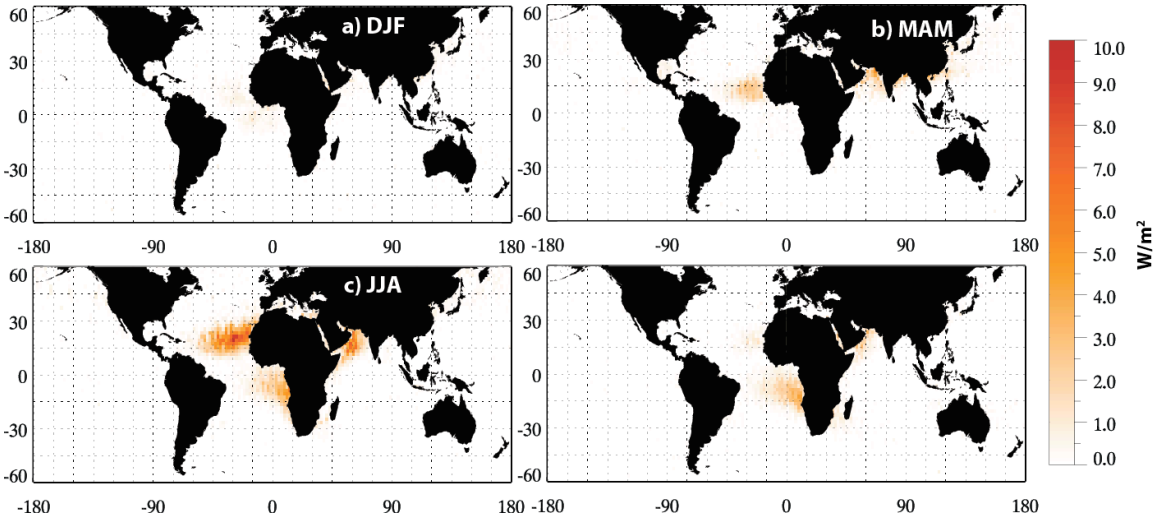

Figure 7 8-year seasonal mean diurnally averaged shortwave cloudy-sky DRE within the atmosphere, using the CALIOP smoke and OBS dust aerosol models. The ACA AOT in the computation is from the CALIOP operational product without any adjustment.

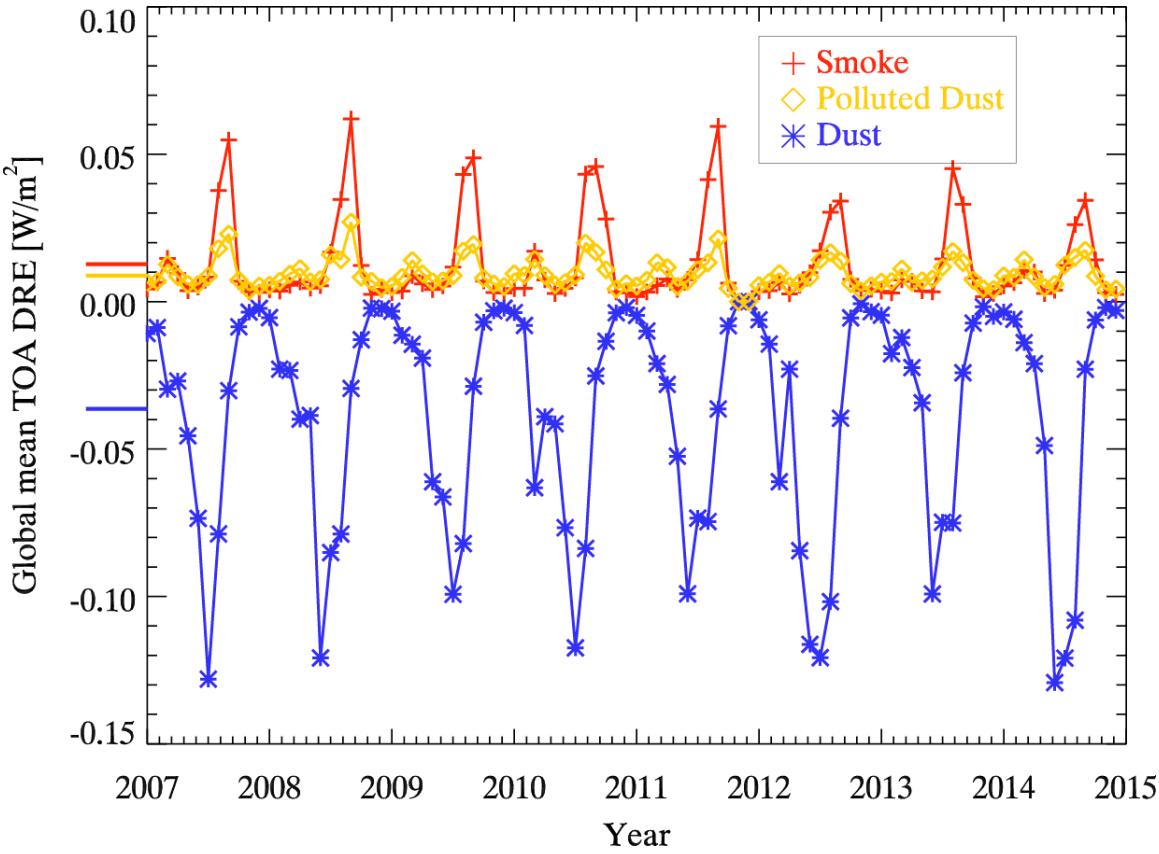

Figure 8 Time series of monthly mean diurnally averaged shortwave cloudy-sky DRE at TOA from 2007 to 2014. The horizontal bars on the y-axis mark the 8-year annual mean values.

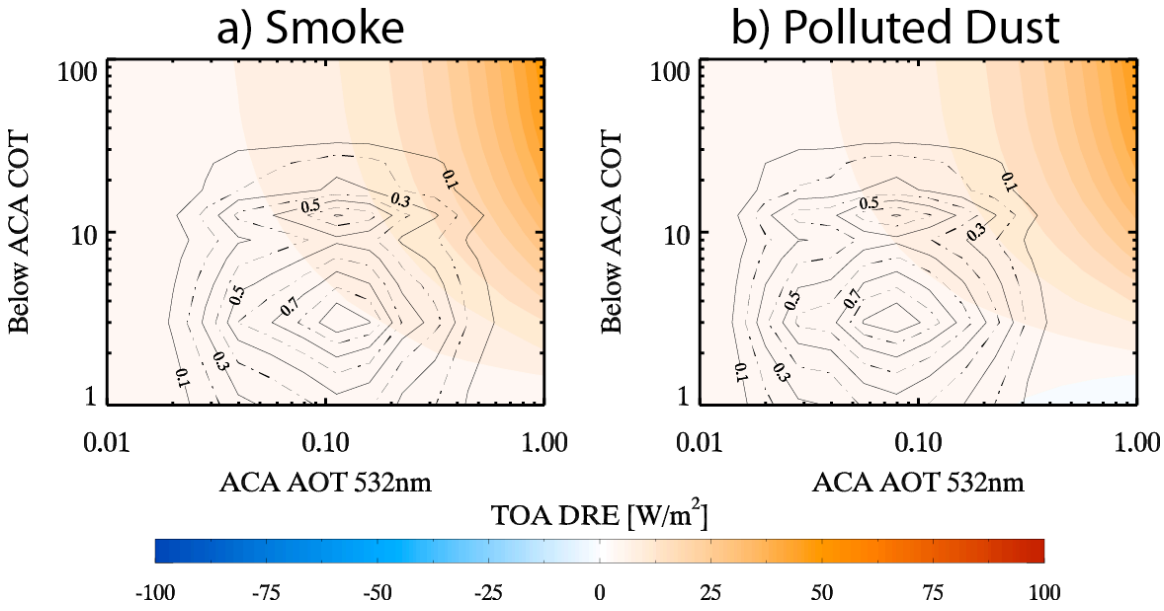

Figure 9 Diurnally averaged TOA above-cloud aerosol DRE as a function of COT and above-cloud AOT for the CALIOP smoke (a) and polluted dust (b) models. Also plotted for each aerosol model are the joint PDFs of above-cloud AOT and underlying COT (line contours); PDFs are obtained from the entire 8-year JJA record for the SE Atlantic region. Here, the solar zenith angle is assumed to be 24° and CER is assumed to be 12.5 μm.

1285

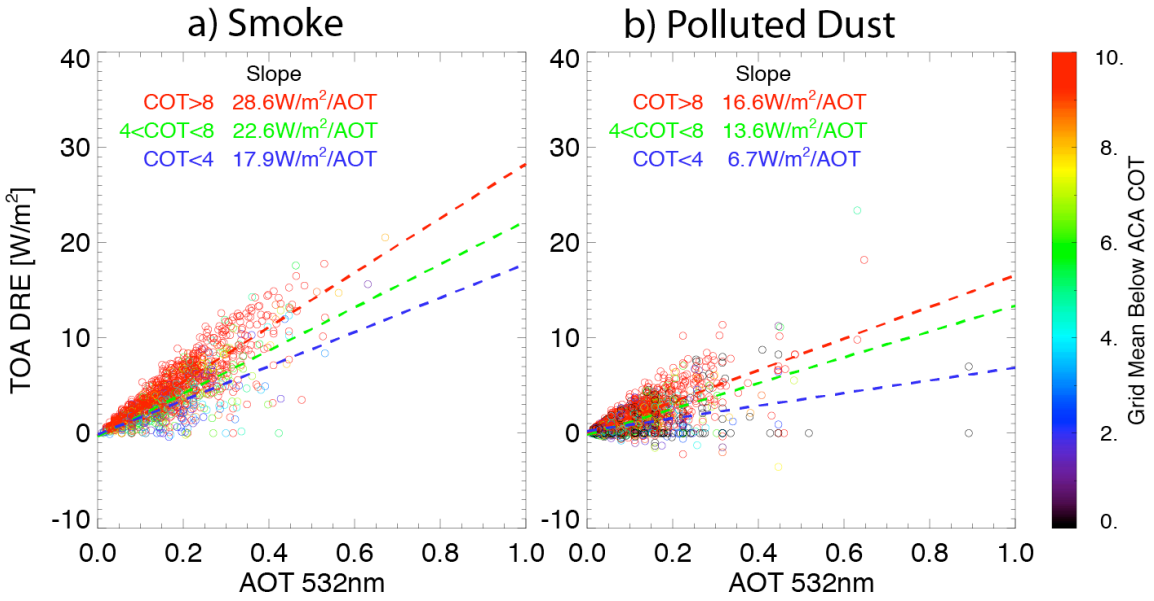

1286

1287 Figure 10 Dependence of grid-mean diurnally averaged DRE at TOA on grid-mean ACA
1288 AOT for a) smoke and b) polluted dust in the SE Atlantic Ocean from 8 years of
1289 CALIOP observations. The colors correspond to grid-mean underlying COT.

1290

1291

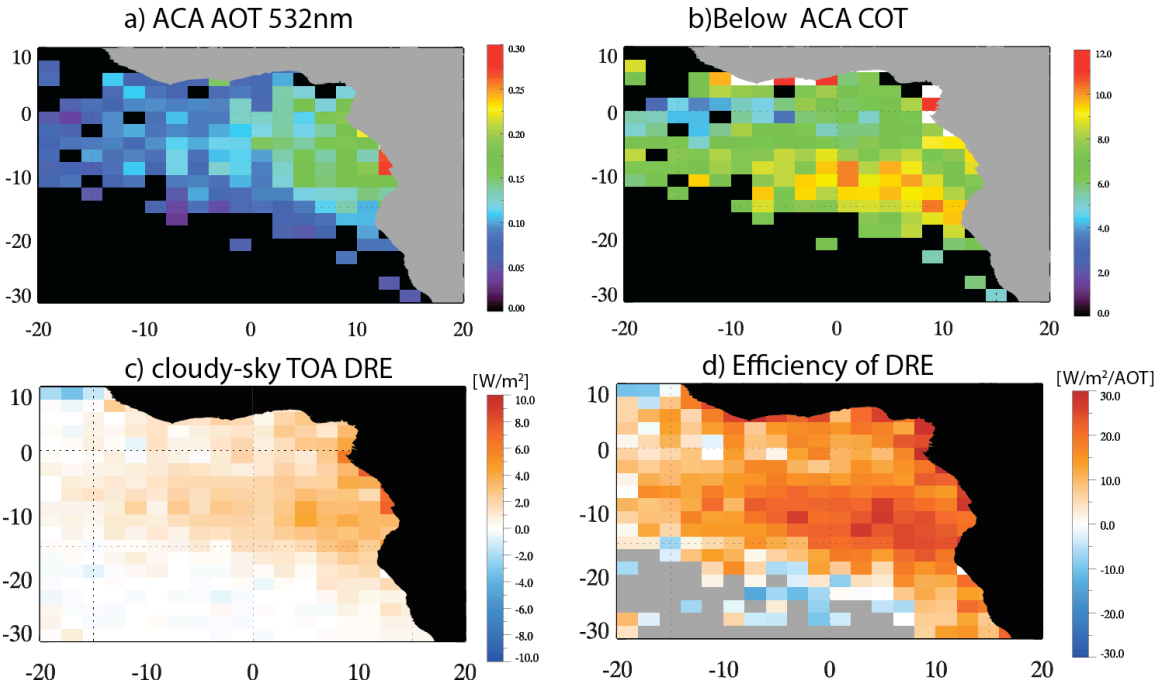

Figure 11 The 8-year seasonal mean (JJA) a) AOT of ACA, b) underlying COT, c) cloudy-sky diurnally averaged DRE at TOA (Wm^{-2}), and d) TOA DRE efficiency ($Wm^{-2}AOT^{-1}$) in the SE Atlantic region.

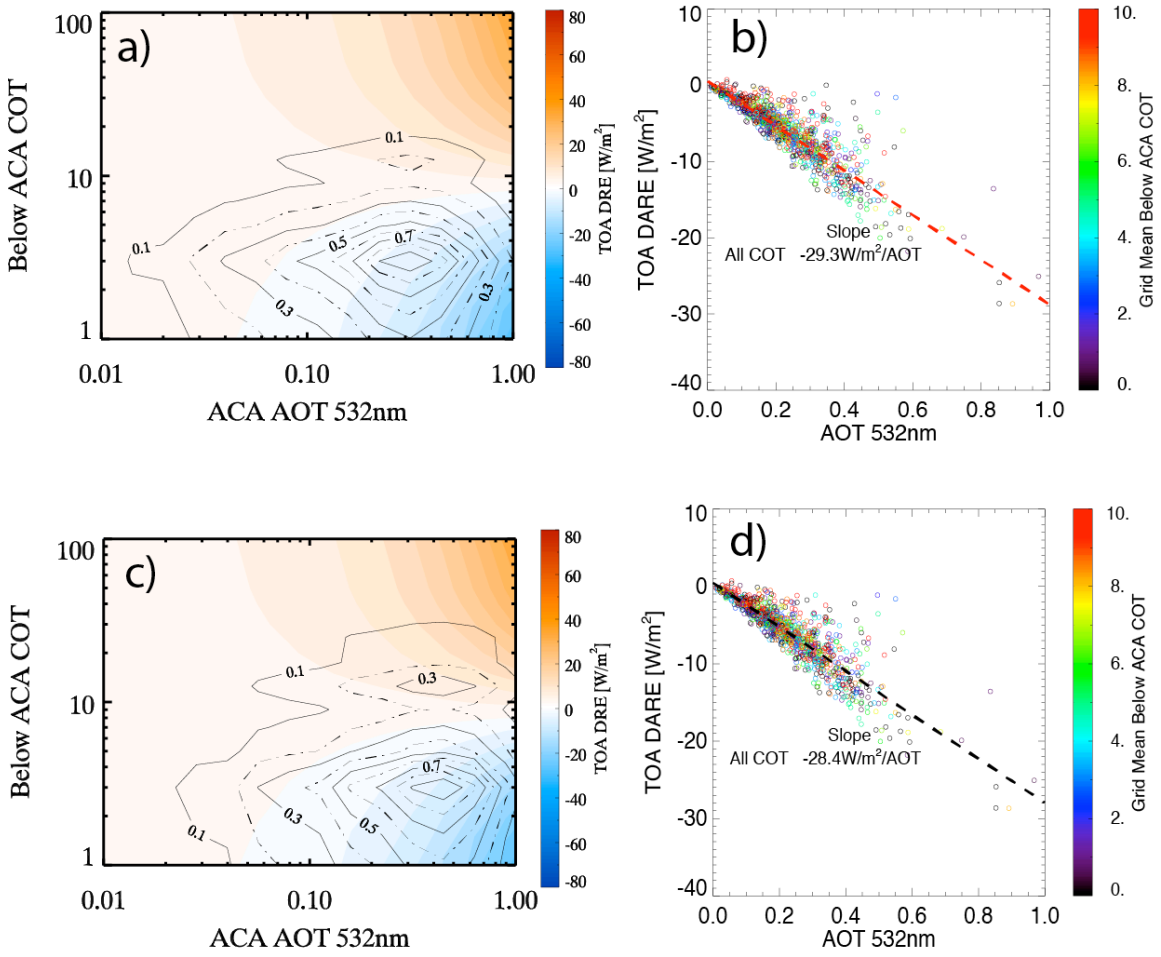

Figure 12: Same as Figure 9 and Figure 10 but for the dust aerosols in the TNE Atlantic region (a and b) and Arabian Sea (c and d).

1304

1305

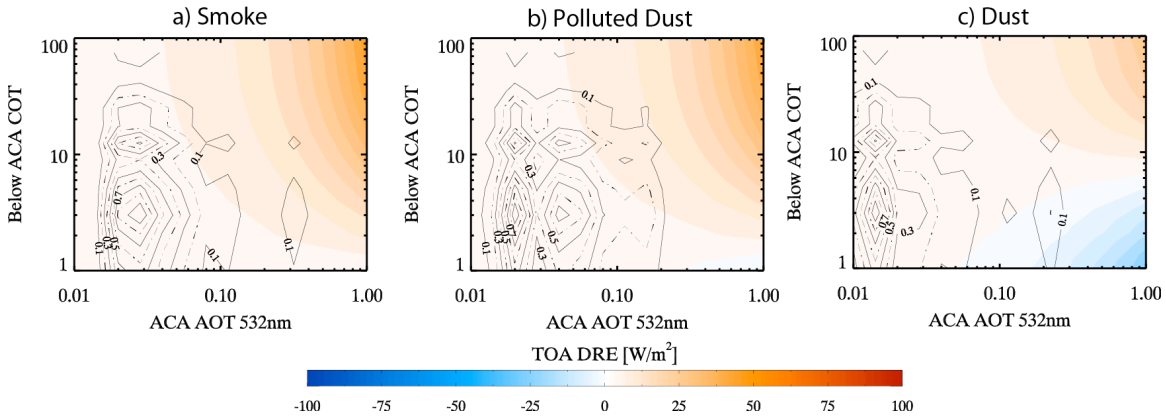

1306

1307 Figure 13 Same as Figure 9 but for the a) smoke, b) polluted dust and c) dust aerosols in
1308 the Northwest Pacific Ocean.

1309

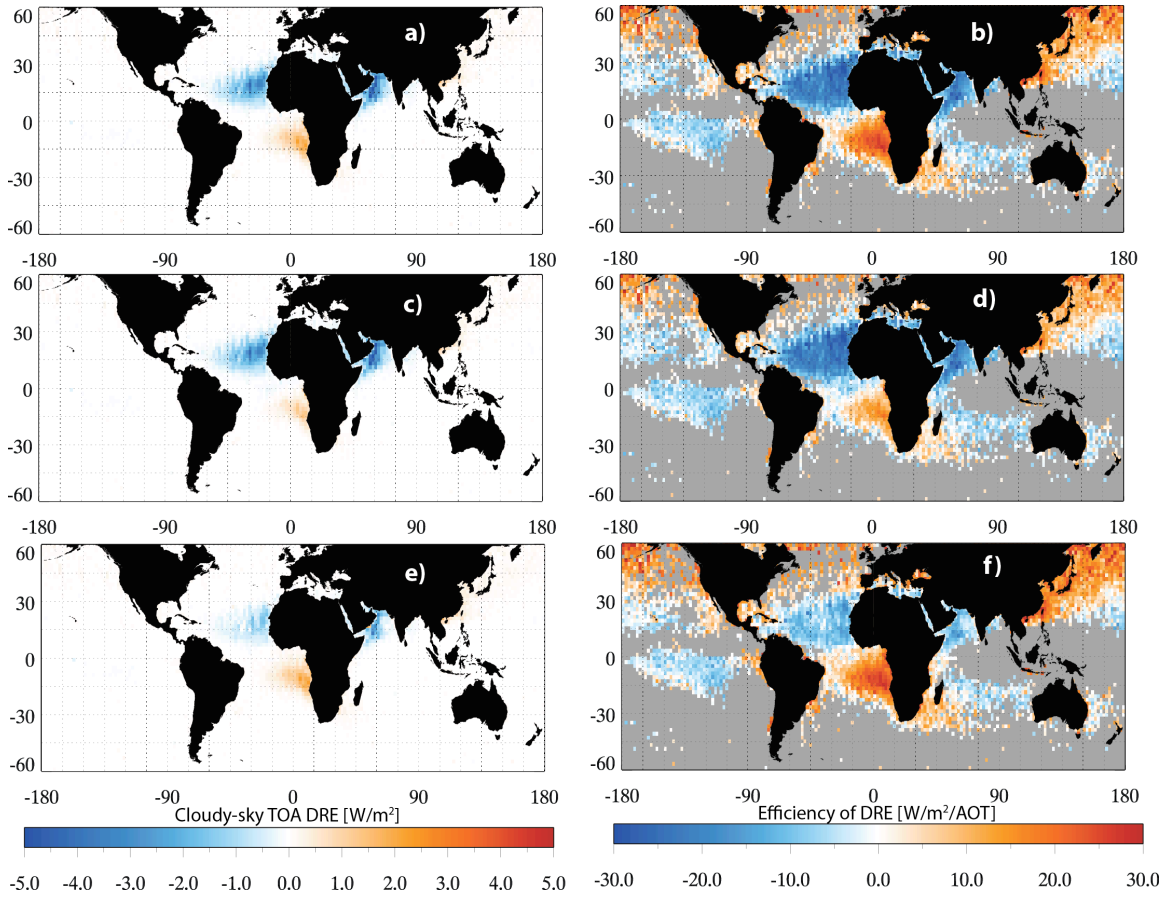

Figure 14 Annual mean cloudy-sky a) DRE at TOA and b) DRE efficiency due to ACA computed using the control run aerosol models; c) and d) are the same as a) and b), except that the CALIOP smoke model has been replaced by the Haywood smoke model; e) and f) are the same as a) and b), except that the OBS dust model has been replaced by the OPAC dust model.

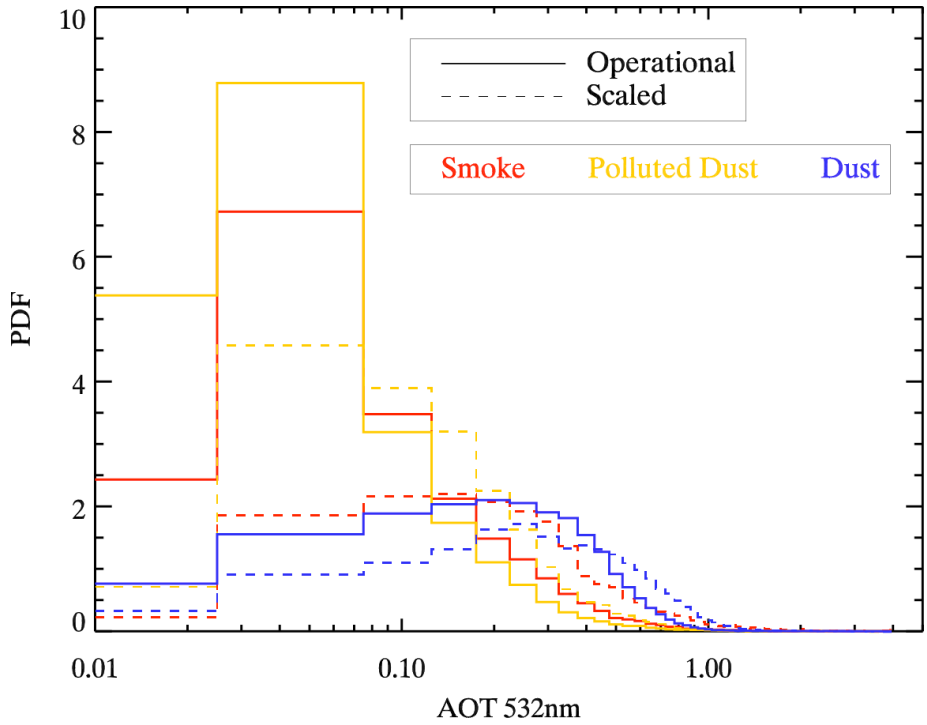

Figure 15 Comparison of the probability density function of above-cloud smoke AOT between the operational CALIOP retrieval (solid) and scaled result based on Eq. (11) (dashed). The comparison is based on one year (2008) of CALIOP data.

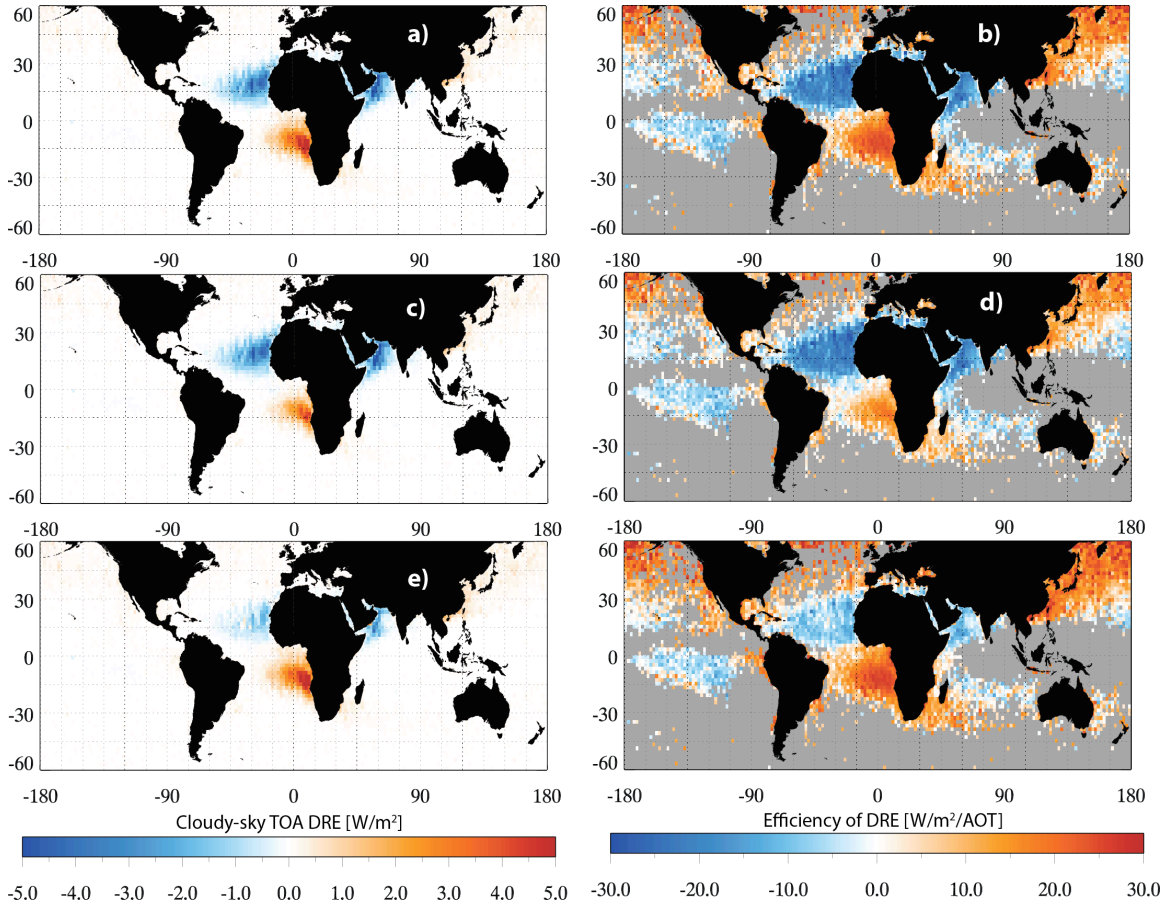

1324

1325 Figure 16 Same as Figure 14, except that the scaled AOT based on Eq. (11) is used in the
1326 computations for smoke aerosols.

1327